SCIENTIFIC COMMITTEE
TWENTY-SECOND REGULAR SESSION
11-19 August 2026
Apia, Samoa (Hybrid)

PROGRESS TOWARDS A NEW SEAPODYM REFERENCE MODEL OF YELLOWFIN TUNA, *Thunnus albacares*, IN THE PACIFIC OCEAN

WCPFC-SC22-2026-SA-IP07
20 July 2026

Submitted by

Lucas Bonnin[1], Inna Senina[1], Romain Forestier[1], Matthieu Lengaigne[2], Karen Guihou[3], Julien Temple-Boyer[3], Kristine Buenafe[4], Joe Scutt Phillips[1], Simon Nicol[1]

[1] Oceanic Fisheries Programme, The Pacific Community (SPC), Noumea, New Caledonia
[2] Institut de Recherche pour le D´eveloppement (IRD), France
[3] Mercator Ocean International (MOI), Toulouse, France
[4] School of Earth and Environmental Sciences, The University of Queensland, St Lucia, QLD, 4067,Australia

Contents

1 Executive summary

1.1 Scope of work

This report describes the progress towards an updated SEAPODYM model for the spatial and temporal dynamics of yellowfin tuna, *Thunnus albacares*, in the Pacific Ocean. This preliminary model uses improved ocean forcing fields, the newest growth and maturity estimations, updated fisheries data structured by a new process defining homogeneous longline strategies, and, for the first time in the yellowfin model, integrates both tagging and larval data into the joint likelihood.

1.2 Key outcomes

While a complete Maximum Likelihood Estimation (MLE), including the estimation of fisheries selectivity parameters, is in progress, current parameterization shows an improvement with respect to the previous reference model, predicting a distinct spatial density patterns: in the equatorial Western and Central Pacific, with a pocket extending North-East towards the coast of Central America, and, towards higher latitudes, in the Kuroshio region and the Coral Sea.

Predictions from this preliminary solution suggest substantial changes in tuna distribution since the 1970s, potentially driven by climate-related changes in ocean conditions. In particular, the model indicates an eastward shift in biomass across the Pacific Ocean, together with a poleward expansion in the northern part of the western and central Pacific Ocean (WCPO).

1.3 Report details

This report documents the development of the updated SEAPODYM configuration for yellowfin tuna in the Pacific and presents the associated calibration, diagnostic, and validation analyses. It describes the model structure, input datasets, and optimization framework used to estimate key biological and fisheries parameters. The report notably summarizes the key steps undertaken during model development to achieve the preliminary reference solution. The report further evaluates model performance against the calibration datasets and a range of independent validation datasets, and examines the resulting spatial and temporal population dynamics, notably in regards to inter-annual ENSO-associated variability and past climate change.

1.4 Main results

1. The updated reference model for yellowfin tuna provides predictions of tuna densities for the 1960–2022 period at a 2° spatial resolution and 30-day temporal resolution, based on the JRA55–NEMO–PISCES hindcast.
2. The model provides a realistic description of spatial distribution of tuna biomass, primarily concentrated within a broad tropical band extending from the western Pacific warm pool across the central Pacific, with distinct northern and southern branches on either side of the equator. Additional biomass hotspots occur at higher latitudes, particularly in the Kuroshio region of the North Pacific and along the East Australian Current in the Coral Sea.
3. Model predictions revealed longitudinal shifts in equatorial biomass associated with ENSO variability, with eastward shift of biomass distributions during El Niño conditions.
4. An eastward shift of unfished equatorial biomass was described over the 50+ years of the hindcast period, together with a poleward expansion in the northern WCPO. These trends are consistent with changes in the location of the western Pacific warm pool and with ocean warming, which has extended thermally suitable habitat towards higher latitudes.

1.5 Remaining actions

Future work will focus on reaching a final reference solution for yellowfin tuna under the JRA55-NEMO-PISCES environmental forcing that was used here, and re-estimating model parameters with an additional ERA5-NEMO-PISCES environmental forcing. These model solutions will be evaluated against an ensemble of Earth System Model forcings bias-corrected from these reanalysis products, to provide an enveloppe of future projections of tuna stock and distributions for various Shared Socio-economic Pathways and up to the horizon 2080.

1.6 Acknowledgements

The continued development and application of the SEAPODYM model to the work of the WCPFC Scientific Committee is facilitated through Project 62. The project affiliates the independently funded work on SEAPODYM into the SC's work programme. It is conducted in collaboration with the Oceanic Fisheries Programme (OFP) of the Secretariat of the Pacific Community. This work under Project 62 was supported by a Climate Change and Tuna Project coordinated by the Oceanic Fisheries Programme at SPC, FAO ABNJ2 Tuna Project funded by the Global Environmental Fund, and by the GCF Regional Tuna Programme, Component B, Activity 3.1.

2 Methods

2.1 Model description

SEAPODYM is a mechanistical eulerian model that simulate tuna movements and population dynamics as a response to oceanic environment (ocean circulation, primary production, dissolved oxygen, water temperature). Parameters of this model are estimated using fisheries (catch, effort and length frequency) and scientific survey data (tagging data, larval CPUE). The model structure and parameter optimization process is described in the *SEAPODYM Reference Manual* and its configuration for several tuna species were presented and updated in previous scientific reports (Senina et al. 2019; Senina et al. 2020).

2.2 Model configuration

2.2.1 Model structure

The SEAPODYM Partial Differential Equations (PDE) from the Advection-Diffusion-Reaction (ADR) model and functional responses to the environment are fully described in the *SEAPODYM Reference Manual*. Four different life stages were considered: i) larvae (age 0–1mo), which mortality is driven by spawning habitat and with passive horizontal movements modeled using advection with surface currents only, ii) small juveniles (age 1–3mo), with mortality driven by feeding habitat and with passive movements modeled using advection with epipelagic currents only, iii) juveniles (age 4–24mo), with mortality driven by feeding habitat and with both vertical and horizontal movement abilities, modeled using both diffusion and advection, and iv) mature adults (age >25mo), with the same modeled behaviour but which contribute to spawning biomass as a function of mortality-at-age. As yellowfin tunas are opportunistic spawners, spawning migrations were de-activated in this configuration, so spawning occured in times and locations of favorable spawning habitat.

Based on the reliability of effort data, two methods were used to compute fishing mortality and predicted catch used in the cost-function: 1) using the Gordon-Schaefer

model and 2) using the Catch-Removal method (*SEAPODYM Reference Manual*). For purse-seine fisheries, effort data was considered as biased, as it is expressed in days and may include time not dedicated to fishing. The Catch-Removal method, independent of effort data, was thus used for these fisheries. The Catch-Removal method was also used for the fishery encompassing all residual gear types, as its effort data was considered as unreliable. For the remaining fisheries, longline and pole-and-line, the effort was used to define fishing mortality and catch predictions, using the Gordon-Schaefer method.

2.2.2 Model updates

Several updates were brought to the SEAPODYM model since the last INTERIM reference model for yellowfin tuna (Senina et al. 2019) and are described in the following section.

Spawning habitat

Two thermal functions were considered for spawning habitat definition: the classical thermal function historically used with SEAPODYM reference models, and a logistic threshold function, allowing asymmetric "hat" with a window of preferred temperatures:

$$f_1(SST;\sigma_1,T_1^*,\sigma_2,T_2^*) = \left(\frac{1}{1+\sigma_1^{SST-T_1^*}}\right)\cdot\left(\frac{1}{1+\sigma_2^{T_2^*-SST}}\right) \quad (1)$$

with T_1^* and T_2^* the respective minimal and maximal temperature thresholds, and σ_1 and σ_2 controlling respectively the slopes of increased and decreased temperature suitability.

Larval data fit

An Early-life (or Larval) cost function component was introduced here, using a gaussian kernel likelihood function, computed from seasonal averages of density of one-month-old recruits D_1 (before transport and mortality) and of observed Larval Density Index LDI, generated from a geostatistical model fitted on larval CPUE data (cf Section 2.4.3):

$$L_E^- = \sum_{s=1}^{N_{season}} \frac{(LDI_s - q_{larvae}.D_{1,s})^2}{2\sigma_{larvae}^2} \quad (2)$$

with q_{larvae} a linear scaling factor, σ_{larvae} the standard deviation of the Gaussian (here fixed and defined as 1), and N_{season} the number of seasons of the aggregation, here four seasons (January-March, April-June, July-September, October-December).

Natural mortality

Natural mortality was redefined to distinguish the amplitude of habitat-dependent mortality between larvae and juveniles/adults, so using two distinct parameters ϵ_0 and ϵ_a. The new formulation of natural mortality is available in Senina et al. (2026b) (page 11).

Catchability

Catchabilities are allowed to vary linearly in time to account for technological advances in fisheries. The new model implementation now enables to estimate this time trend. The catchability formula was defined as:

$$q = q_{t0} + a \cdot t \tag{3}$$

with both the initial catchability value q_{t0} and the slope a estimable in the MLE.

2.2.3 Static model parameters

Fisheries selectivity parameters were not included in the parameter optimization process and fixed to values set *a priori* from fisheries-specific total length distributions. Two types of selectivity functions were considered here, i) a sigmoid-shape function (or type II) for longline fisheries and other gear types, parameterized by a threshold length $\hat{l}_f$ and a slope coefficient ς_f, and ii) a asymetric gaussian function (or type III) for purse-seine and pole-and-line fisheries, parameterized by mean $\hat{l}_f$, standard deviation σ_f and asymptotic value at large fish size μ_f. Fisheries-specific selectivity parameters values are described in Appendix Table 3.

Some model parameters cannot be estimated from data with the current model implementation and must be defined *a priori*: length-at-age, weight-at-age and maturity-at-age. The growth and maturity models from the 2023 MULTIFAN-CL assessment report (Magnusson et al. 2023) were used to interpolate lengths and proportion of mature individuals to the model monthly age structure. *Von Bertalanffy* parameters from OFP-SPC (2019) were used to compute weight-at-age from length-at-age.

2.2.4 Numerical configuration

The SEAPODYM PDE from the ADR model were solved numerically at a 2.5 day time step (with a solution extracted at monthly time step) and on a 2x2° regular grid covering the spatial domain of the Pacific Ocean (100°E-70°W and 59°S-61°N). Neumann boudary conditions were considered. Monthly age classes covered the 82 first months of life, an additional A+ class was defined to collect the remaining population density.

For the MLE runs, the Indian Ocean was closed and a buffer zone was specified in the Indo-Pacific region to prevent from biomass accumulation due to closed boundary, enabling the solution to focus on fitting observed data on the Pacific Ocean domain. For the final simulation runs used for model diagnostics and validation, the Indian Ocean was opened back and the buffer zone was removed.

First optimization runs were based on the previous yellowfin tuna reference INTERIM solution (Senina et al. 2019), both for parameter starting values and for initial conditions. Along model development process, initial conditions were redefined from intermediate

solutions. In any case, a period of 5 years was systematically considered before cost-function computation, to enable the population to stabilize and prevent the MLE from being inmpacted by initial conditions.

2.3 Environmental forcing data

The environmental forcing was generated with the NEMO-PISCES ocean and geochemical model, forced by the JRA55 atmospheric reanalysis product (Japanese 55-year Reanalysis: Kobayashi et al. (2015)). Sea temperature, dissolved oxygen, and zonal and meridional currents were averaged over 3 vertical layers, based on euphotic layer depth (0-1.5.zeu/1.5-4.5.zeu/>4.5.zeu). This dataset was prepared by the French Institute for Sustainable Development, providing a global gridded product on a 1x1° grid, at a monthly time scale over the 1958-2022 period. Tuna forage fields, defined for six functional groups based on vertical layer and vertical migration behaviour, were prepared by Mercator Ocean International (https://www.mercator-ocean.eu) and provided on the same spatio-temporal grid. A more detailled description of the ocean forcing production is available in Senina et al. (2025).

In order to reduce computation time and memory use to a reasonable scale, the model was configured over a 2x2° spatial resolution, and forcing fields were degraded to match this spatial grid.

2.4 Tuna data

2.4.1 Fisheries data

Industrial fishing fleets for yellowfin tuna use three main fishing gears, purse-seine, long-line and pole-and-line, with purse-seine catch representing most of the total catch (Figure 1). SEAPODYM requires geolocated catch and effort data, for computing both local fishing mortalities and predicted catch for parameter estimation. Except for the years 2021 and 2022, which were not included in the training data used for MLE, geolocated catch data matched total landings from SPC Yearbooks (OFP-SPC 2025), ensuring a complete description of fishing mortalities in the model.

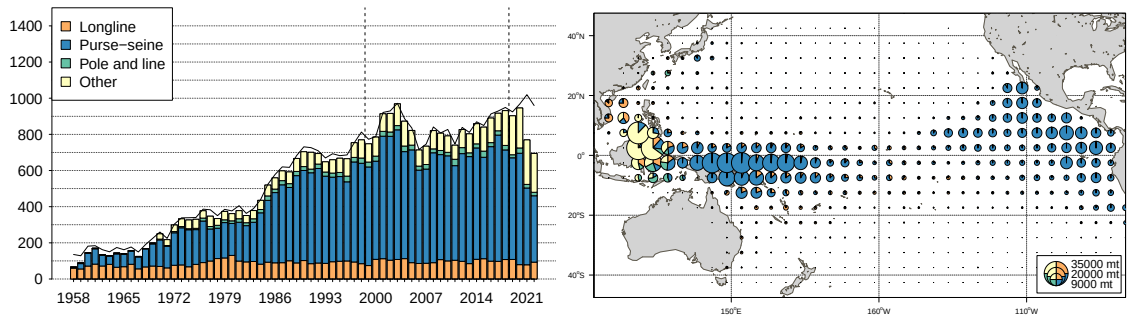

Figure 1: Total annual yellowfin catch aggregated by gear. a) Annual catch per gear type, with vertical dashed lines representing the MLE period and the solid black line indicating total landings from SPC Yearbook data. b) Spatial distribution of catch per gear type over the MLE period.

Catch-effort data were integrated at the monthly scale and with 1° or 5° resolution. Length-frequency data were integrated at the quarterly scale with variable resolutions ranging from 1x1° to 10x20°. A description of catch and length-frequency data coverage is available in Appendix Figure 20. Fisheries data were aggregated into groups of similar fishing strategies, defined within the model as groups of specific capturabilities and selectivities, and hereafter called "fisheries". Purse-seine fisheries were defined using schooling type (free schools, floating object association, marine mammal association) and ocean basin, resulting in 7 distinct fisheries (cf Appendix Table 4). An additional purse-seine fishery was defined to collect all data with poor quality standards. Pole-and-line fisheries were defined based on flag, period, and ocean basin, resulting in 7 fisheries. Longline fisheries were defined using data quality, species composition and latitude, using a *Kmeans* clustering algorithm, following the methodology described in Forestier et al. (2026), resulting in 6 distinct fisheries. All data associated to other gear types were pulled into a last fishery. A summary table of fisheries definition is available in Appendix Table 4.

Fisheries data were splitted in three datasets, a training dataset used for MLE, over the 1999-2018 period, and two independent datasets used for model validation, over the 1982-1998 and 2019-2022 periods.

2.4.2 Conventional tagging data

Conventional tagging data consisted in geolocated, aged and timed release-recapture pairs. Tagging data corresponding to releases in the WCPO and EPO were respectively obtained from the Pacific Community and the Inter American Tropical Tuna Commission. They were filtered to remove pairs with i) no release length recorded, ii) recaptures with relocation reliability lower or equal to 5° and with dating reliability lower or equal to the quarter, iii) release and recapture on the same date, and iv) average speed greater than 1 knot.

Among this dataset, release-recapture pairs were assigned to groups with common recapture month, hereafter called "tagging cohorts". This tagging dataset was splitted in a MLE dataset used for model calibration and an independent dataset used for model validation. The optimization dataset consisted in high quality and quantity data, consisting in tagging cohorts with a minimum of 50 tags, and with recaptures between 2006 and 2012. The rest of the tagging cohorts, with a minimum of 10 tags, were assigned to the validation dataset. The MLE dataset encompassed 12962 tags, while the validation dataset encompassed 2510 tags. History of tag releases, and distributions of time-at-liberty, length at release and length at recapture are available in Appendix Figure 21.

2.4.3 Larval data

Probability of larval presence were obtained from a geostatistical model (Buenafe et al. 2022) to be used as a proxy for larval density observations, and hereafter refered to as Larval Density Index (LDI). This dataset consisted in an index between 0 and 1, available

on a 1x1° grid and at a seasonal scale (4 seasons: January-March, April-June, July-September, October-December). Here, geostatistical model predictions were subsampled on the same 2x2° grid as the environmental forcing (cf Section 2.3).

2.5 Model calibration

SEAPODYM model calibration, i.e. the estimation of model parameters, is based on a Maximum Likelihood Estimation approach (MLE), using a Quasi-Newton algorithm to minimize a cost-function computed to quantify fit between observations and model predictions. The cost-function was defined as the negative logarithm of four likelihood functions, corresponding to the four observational datasets: Catch(-Effort) (C), Length-Frequency (L), Tagging (T), and Early-life or larval (E).

Catch likelihood was calculated considering a Poisson distribution for catch data from longline and pole-and-line fisheries, and considering a Normal distribution for catch data from purse-seine and other gear type fisheries. Length-frequency likelihood was calculated using relative observed length frequencies considered to follow robustified normal likelihood. Tag and Larval likelihoods were calculated with tag recapture density and Larval Density Index considered to follow Normal distributions.

The resulting cost-function was defined as $L^- = L_C^- + L_L^- + L_T^- + L_E^- + \beta$, with the additonal β penalty term, called the *biomass constraint*. The biomass constraint is used to prevent the model from finding a solution with unrealistically high biomass, which would enable a perfect fit to catch-data from Catch-Removal fisheries. This biomass constrain is defined as:

$$\beta = \left(\left(\frac{1}{n_t} \sum_{(i,j)\in\Omega, t\in\{1,nt\}} B_{i,j,t}^{pred} \right) - \overline{B} \right)^2 \tag{4}$$

with $\overline{B}$ a specified mean stock biomass value, and Ω a rectangular domain. $\overline{B}$ and Ω were modified along model development, with a final setting of $\overline{B} = 6.6Mt$, and $\Omega = \{120E - 150W, 35S - 45N\}$.

2.6 Diagnostics and validation

2.6.1 Diagnostics

The assessment of the performance of a SEAPODYM solution is a complex task, as model predictions must be evaluated against four observational datasets, across space, time and age, and for each individual fisheries. For each data type, fit metrics were selected to best summarize the information across these different scales, either as global scores or as spatially explicit maps of model performance.

For catch data, Taylor diagrams were used to summarize spatiotemporal fit (time x lon x lat) into three metrics: Pearson correlation (R^2), variance ratio (VR) and Normalized Root Mean Square Error (NRMSE). Normalization of RMSE was perfomed using standard deviation of observations. A solution was considered as robust when showing $R^2>0.7$, $0.8 < VR < 1.2$ and $NRMSE < 0.5$, and still considered as fair when showing $R^2>0.5$, $0.6 < VR < 1.4$ and $NRMSE < 0.7$. Further strata description was brought by extracting these taylor metrics at different regional scales and for different groupings of fisheries, for instance by focusing on fisheries using effort-based catch prediction separately.

To identify potential local misfits, three metrics were computed at the grid-cell level to provide visual spatial maps of model performance: Pearson R^2, R-Squared Goodness-of-Fit (RSGF) and Relative Error.

At the fishery scale, time series of residuals between total observed and predicted catch were analyzed using a linear model to identify any systematic bias (high intercept) and residual trend (high |slope|). For effort-based fisheries, such insconsistencies can be symptomatic of a failure to estimate catchability and its time trend.

In order to assess fit to length-frequency data, predicted age-distribution were aggregated across space and time at the fishery level and converted to length distributions. Bias of mean lengths was assessed using Standard Mean Difference (SMD), computed as the difference between observed and predicted mean length, standardized by the root sum of variances. A |SMD| score was considered as good when <0.5 and fair when <0.8. The difference in shapes of length distributions was quantified using NRMSE, computed as the RMSE between proportions of fish in length bins, standardized by the observed mean length. A NRMSE score was considered as good when <0.5 and fair when <0.7.

The fit to tagging data was assessed using longitudinal and latitudinal profiles of tag recaptures, focusing on the 20°S-20°N band where most of the tag recaptures were observed, and distinguishing between WCPO (west of 150°W) and EPO (east of 150°W). NRMSE was used to assess the difference between the shapes of observed and predicted profiles, with scores <0.5 and <0.7 respectively considered as good and fair. Kling-Gupta Efficiency (KGE) was computed as well to quantify goodness-of-fit of profiles, with scores >0.7 and >0.5 respectively considered as good and fair.

The fit to larval data was assessed at the spatial, seasonal and environmental scale. Seasonal profiles of LDI (cf Section 2.4.3) and predicted larval density were extracted in different rectangular regions and Pearson R^2 and RMSE were computed. LDI and larvael density distributions were projected onto four environmental covariates: SST, primary production (proxy for larvae prey density), and epipelagic micronekton (proxy for predator density), which are involved in spawning habitat definition, and dissolved oxygen in the upper-mesopelagic layer, which constrains adults ability to dive in deeper water for thermoregulation during spawning. Divergence between environmental profiles were assessed using NRMSE, with scores <0.5 and <0.7 respectively considered as good and fair.

More complete descriptions and definitions of diagnostics and statistical metrics of fit used to evaluate SEAPODYM reference models performance are available in Senina et al. (2026b).

2.6.2 Validation

Model selection and validation relied on two criteria: i) the pertinence of modeled biological processes; and ii) how it performs with independent datasets.

The pertinence of modeled biological processes was mainly assessed by comparing estimated values of model parameters with the literature.

Archival tag data from Project 42 (OFP-SPC 2026) was also used to assess the pertinence of modeled biological processes. Specifically, an hypothesis was made on the description of tuna vertical behaviour: tunas would tend to limit their vertical use to shallower water in areas/time with strong vertical temperature gradient. In order to better describe such a behaviour, the epipelagic layer temperature was corrected to bring it closer to SST when such a gradient is strong. archival tag data was used to investigate the existence of such a behaviour for yellowfin tuna, by analyzing depth use in relation to vertical thermal gradient from ocean forcing field.

The estimated thermal habitat was also compared to temperature distributions from archival tags. To do this, SEAPODYM mean layer temperature was computed as the average of the three layers' temperature, weighted by each layer contribution to feeding habitat (considering forage and age-dependent accessibility), which is designed to depict the propotion of time tunas spend in each layer. This mean temperature was then weighted by tuna density to get age-specific mean temperature, which was compared to archival tag age-specific mean daily temperature. The archival tag data sampling was not balanced across ages, showing two modes of ages. Two age groups were thus defined ($>40mo$ and $<40mo$) to compare temperature distributions between archival data and SEAPODYM data. Temperature distribution from SEAPODYM data were weighted to reproduce the age-sampling of archival tag data and thus prevent from the influence of sampling bias.

The performance of a model was also assessed by examining how it performed when using independent datasets, i.e. data that was not used in the MLE. Fisheries data on two time windows before and after the MLE were used for validation. Here two time periods were considered for validation: the 1983-1999 and the 2019-2022 time windows. Such assessment required to re-estimate capturabilities starting value and slope for fisheries that used effort-based prediction method, while keeping the model parameters fixed. The independent tagging dataset consisted in tags not used in the MLE (cf Section 2.4.2).

3 Results

3.1 Chronology of model development

First model optimization runs were performed using a cost function with fisheries data only. The MLE solution showed more constrasted tuna distribution than in the previous INTERIM reference model. Adult densities concentrated in distinct hotspots, except in the Eastern Pacific Ocean (EPO) that showed diffuse densities because of low feeding habitat quality (cf Appendix Figure 22 Panel a).

The introduction of tagging data in the cost-function(CLT) first resulted in a MLE that showed very poor fit to fisheries data. The following experiment was performed by down-weighting tagging data contribution to the cost function. This MLE showed better fit to catch data, length frequencies and tagging data than the CL MLE solution. Adult density distribution differed from the CL MLE solution, with three hotspots in the WCPO (Kuroshio region, Central tropical pacific and coral sea) and EPO densities concentrated in coastall regions (cf Appendix Figure 22 Panel b). The solution lacked biomass in the offshore EPO, thus showing a very poor fit to catch in this region, especially to the purse-seine fisheries S5 and S7. The S5 fishery notably showed an anomaly in the early 2000's, due to a failure of available biomass to support increased catch observed during this period. This solution was charecterized by lower directed movements, stronger habitat-dependent mortality and an unrealistic thermal habitat characterized by a 36°C thermal optimum and very high thermal range ($\sigma_m = 12$°C).

Then, larval data was added to the cost function within the ultimate CLTE optimization experiments. Special attention was paid to the thermal habitat definition. Fixing the thermal range to a lower value ($\sigma_m = 2.5$) notably resulted in an alternative solution with a more realistic thermal optimum of 33.5°C, and a higher biomass in the EPO able to support catch in this region (cf Appendix Figure 22 Panel c). Yet, this MLE seemed unrealistic as it used two different mechanisms to explain WCPO and EPO catches: high EPO densities supported by high recruitment due to higher spawning habitat, and high WCPO densities supported by good feeding habitat quality. Higher recruitment in the EPO was achieved by increasing the predator function, resulting in a biologically irrelevant shape, with spawning habitat quality increasing with predator density. High estimated diffusion also enabled densities to spread in the EPO and fit to catch data.

As optimization struggled to find a pertinent solution to describe thermal habitat and EPO catch, the current forcing data, and specifically the epipelagic layer temperature, was suspected to be unable to describe tuna environment. Indeed, the EPO is characterized by a strong vertical thermal gradient, and yellowfin tunas are known to use shallower water in such environment (cf variations of vertical behaviour with Mixed Layer Depth in Schaefer et al. (2007)). In order to provide a more pertinent description of tuna's environment, the epipelagic temperature forcing was corrected to get closer to SST when vertical thermal gradient is strong (Appendix Figure 23). The correction is described in Appendix Section 7.3 and hereafter called T_{L1}^{cor}.

New CLTE optimization experiments were thus performed using this T_{L1}^{cor} corrected forcing. They resulted in a better estimation of the feeding habitat and movement parameters, and thus in a better fit to EPO catch. Indeed, the thermal habitat was characterized by a more pertinent optimal temperature for oldest ages (26.6°C) and with a narrower thermal range ($\sigma_m = 4.5$°C). The fit to EPO purse-seine fisheries catch was greatly improved (cf Figure 2), with higher EPO biomass able to support the increased catch by the S5 fishery observed in the early 2000's.

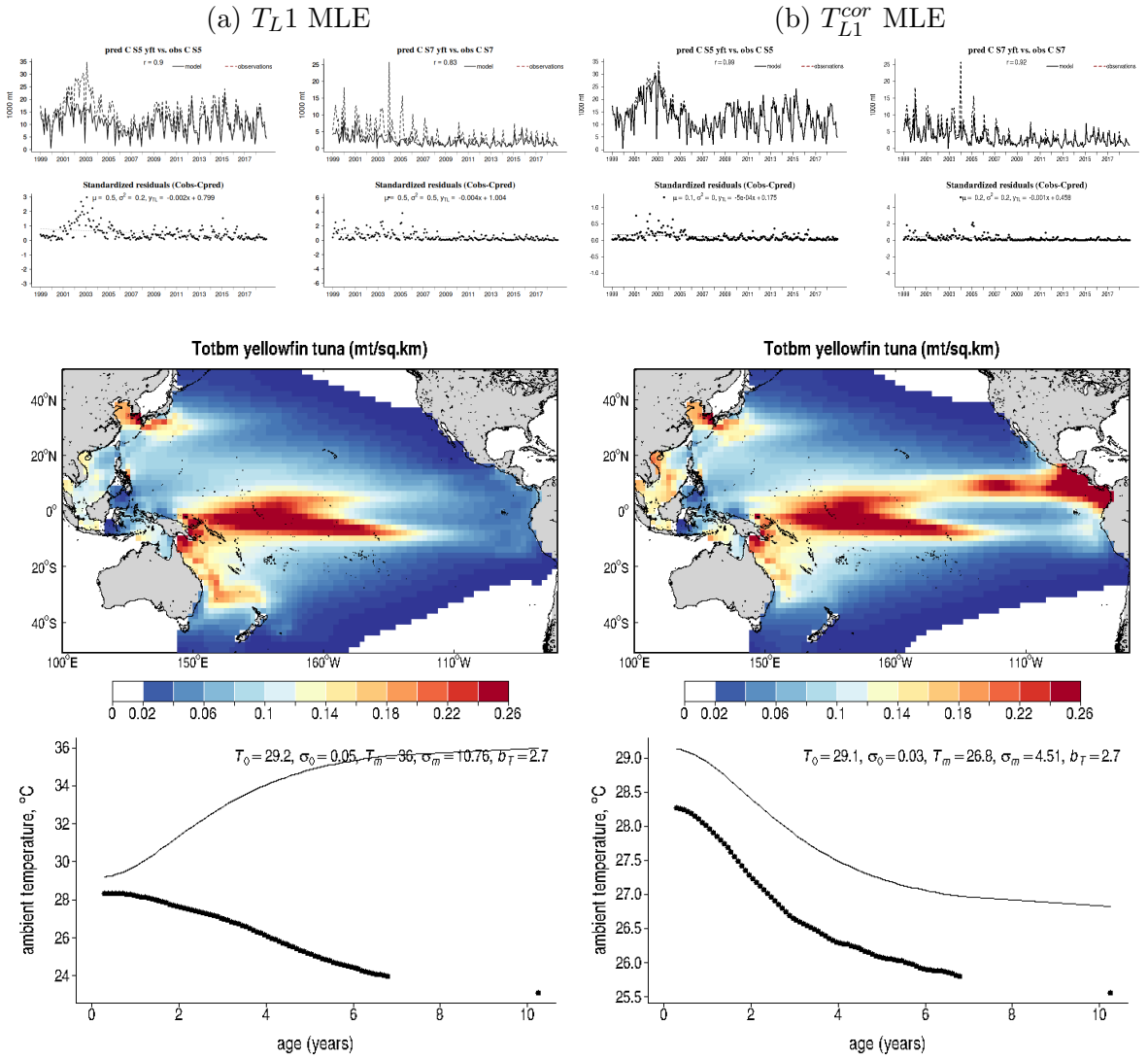

Figure 2: Impact of epipelagic temperature correction on the MLE and the fit to EPO catch. Feeding habitat and movement parameters were estimated here, using the regular T_{L1} or the corrected T_{L1}^{cor}, where epipelagic temperature is brought closer to SST when vertical thermal gradient is strong.

However, a very high thermal range estimated for the spawning habitat lead then to reconsider the gaussian shape of the function. For following optimization runs, an asymetrical double logistic threshold was thus considered for the thermal function of the spawning habitat.

Further optimization runs and the interpretation of their outputs lead to reconsider the reliability of the input fisheries data. First, a failure of the model to fit the dual mode in length frequencies observed for the P11 fishery lead to reconsider the definition of this fishery. Indeed, a deeper look into the spatial distribution of mean lengths within this fishery lead to identify a different fishing strategy during the year 2006 (cf Appendix Figure 24). The year P11 fishery was thus splitted into a P110 (<2006) and P111 fishery (2006). But most importantly, length-frequency data from the S7 fishery (EPO Purse-Seine on free schools) showed a second mode with unrealistically large fish ($120cm$) for a purse-seine fishery. An error in the preprocessing of length-frequency data resulting in the removal of high fish count samples was spotted and fixed. The new processing resulted in ∼40 times more fish sampled for this fishery, resulting in a more realistic length-frequency, with a lower proportion of large fish (Appendix Figure 25)

Next optimization runs with corrected fisheries data resulted in an MLE with an improved fit to fisheries and tagging data. Yet, two correlated issues remained: i) the estimated mortality was characterized by an unlikely low mortality of early life stages (∼0.2 mo^{-1} for the first age class); and ii) spawning habitat showed very low values (cf Appendix Figure 22 Panel d). These issues likely resulted from a faulty definition of mortality parameter bounds, with the solution reaching a given recruitment using low spawning habitat, by default of using higher baseline natural mortality of larvae.

In the final optimization runs, bounds of mortality parameters were expanded and enabled the solution to reach another equilbrium with a more pertinent high baseline larval mortality and higher spawning habitat values (cf Appendix Figure 22 Panel d).

A deterioration of tag fit metrics in the latest optimization runs lead to test the impact of the correction of movement parameters on overall data fit metrics. Starting from the MLE, movement parameters were either left as is ($V_m = 0.53$ and $\sigma = 2.0$) or modified to a previous good solution that presented good catch fit metrics ($V_m = 0.21$ and $\sigma = 0.5$). Capturabilities and their slopes were then re-estimated over the optimization period and the two validation periods. Larval, tag, catch and length frequency fit metrics over the optimization and independent datasets were then compared. The model state with corrected movement parameters, which thus cannot be considered as an MLE, presented the best overall compromise between the different data fit metrics, notably with better tag, larval and LF fit metrics than the corresponding MLE.

3.2 Diagnostics and validation

Using the best solution obtained during model development (cf Section 3.1), model performance was assessed against both the optimization and independent validation datasets. Table 1 summarizes the fit metrics for each data type and dataset.

Table 1: Summary of fit metrics from the best model solution. Fit metrics associated to each data type is presented here. For catch data, metrics were computed for all fisheries combined or for effort-based fisheries only. For LF data, weighted averages of fisheries-specific metrics were computed, using the number of samples as weights. For tagging data, overall spatial fit metrics are provided, as well as fit metrics corresponding to longitudinal and latitudinal profiles (cf Figure 7). For larval data, fit metrics are provided for the distributions of observed and predicted larval density across four environmental fields: surface temperature, oxygen concentration, primary production (prey density) and epipelagic micronekton (predator density). For fisheries data, two validation datasets were considered, corresponding to the pre-MLE 1983-1998 period and the post-MLE 2019-2022 period. For tagging data, a single validation dataset was considered, and for larval data, no validation dataset was considered. Color coding represent good (green), fair (yellow) and bad (red) fit metric values.

			Dataset		
			MLE	Validation	
Data type		Metric			
Catch	All fisheries	R^2	0.9	0.93	0.83
		Var.ratio	0.72	0.8	0.56
		NRMSE	0.34	0.27	0.44
	Effort fisheries only	R^2	0.53	0.56	0.55
		Var.ratio	0.69	0.95	0.7
		NRMSE	0.69	0.7	0.68
Length	All fisheries	NRMSE	0.45	0.66	0.49
		SMD	0.01	0.09	-0.01
Tagging	Overall	R^2	0.8	0.85	
		Var.ratio	0.5	0.43	
		NRMSE	0.49	0.47	
	Trop. lon. profile	NRMSE	0.329	0.265	
		KGE	0.85	0.82	
	WCPO lat. profile	NRMSE	0.382	0.385	
		KGE	0.81	0.74	
	EPO lat. profile	NRMSE	0.627	0.35	
		KGE	0.56	0.84	
Larval	SST	NRMSE	1.42		
	O2	NRMSE	0.42		
	PP	NRMSE	0.38		
	MNK	NRMSE	0.36		

3.2.1 Catch fit metrics

The model shows good fit to the total catch and to the total catch by region (Figure 3). The region R1 (Kuroshio region, South-East of Japan, cf Figure 8), shows slightly worse correlation and error, but with scores that can still be considered as fair. The overall good fit to catch data is maintained when considering validation datasets, i.e. datasets independent from the data used in the MLE.

The fit to catch by the effort-based fisheries is relatively poorer, with poorer correlation and error, but with scores that can still be considered as fair (Figure 4).

(a) MLE - 1999-2018 (b) 1983-1998 (c) 2019-2022

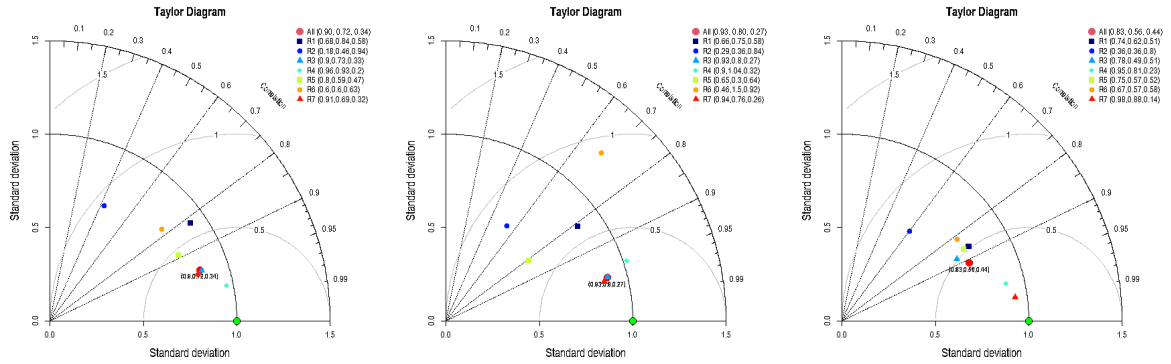

Figure 3: Fit to catch data - all fisheries combined. Taylor diagrams provide three aggregated metrics of fit to total catch (red dot) or regional catch: Pearson correlation, variance ratio and NRMSE. The fit metrics are provided for the optimization dataset, over the 1999-2018 period, and for the two independent validation datasets, over the 1983-1998 and 2019-2022 periods.

(a) MLE - 1999-2018 (b) 1983-1998 (c) 2019-2022

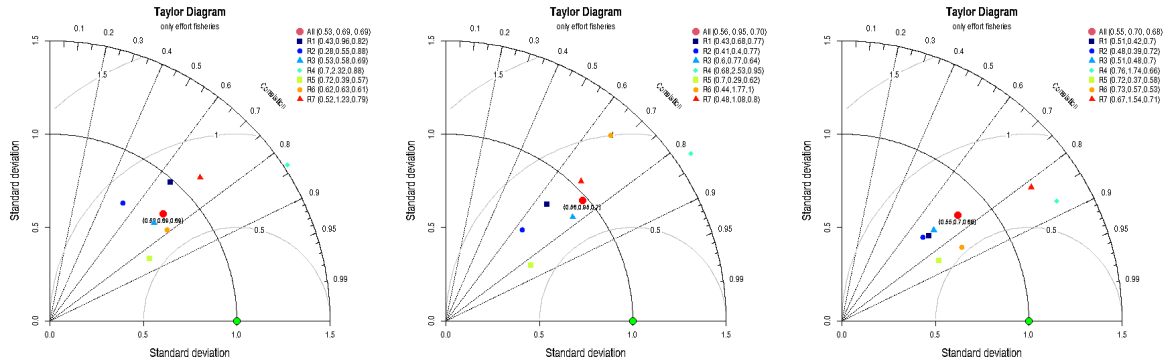

Figure 4: Fit to catch data - effort-based fisheries only. Taylor diagrams provide three aggregated metrics of fit to total catch (red dot) or regional catch: Pearson correlation, variance ratio and NRMSE. The fit metrics are provided for the optimization dataset, over the 1999-2018 period, and for the two independent validation datasets, over the 1983-1998 and 2019-2022 periods.

Spatial patterns of goodness-of-fit, correlation and error with total observed catch are displayed in Figure 5. The model shows good fit metrics in location with high observed

catch, and this for both MLE and independent validation datasets. An exception to this performance can yet be noticed in the region south of Japan, around 20°N, where the model fails to predict sufficient catch when compared to the 1983-1999 independent dataset, which results in lower goodness-of-fit and higher relative error.

(a) MLE dataset - 1999-2018

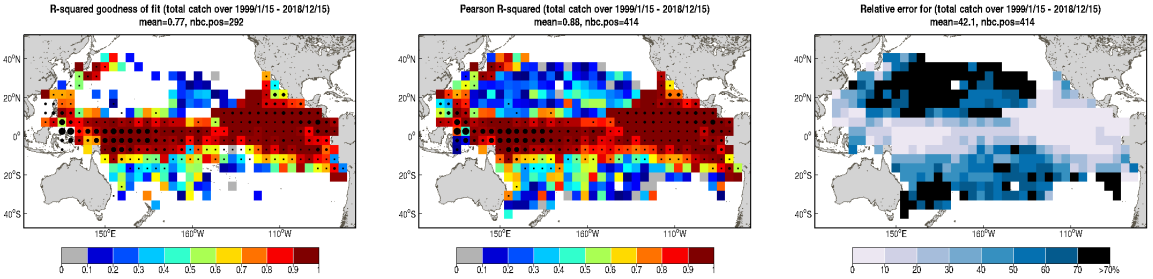

(b) Validation dataset - 1983-1998

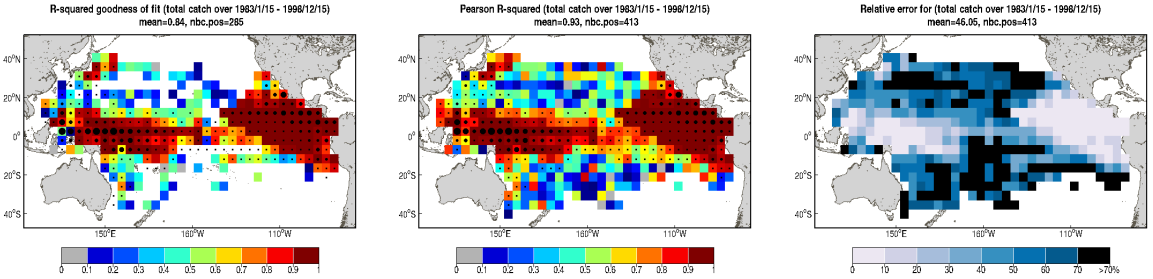

(c) Validation dataset - 2019-2022

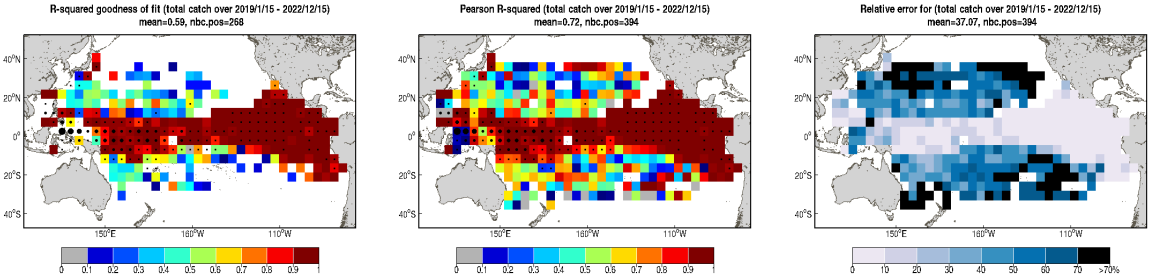

Figure 5: Maps of fit metrics - all fisheries combined. R^2 goodness-of-fit, Pearson R^2 and relative error between total predicted and observed catch were computed for each spatial grid cell. Black dots represent local observed catch.

3.2.2 Length frequencies fit metrics

Most of the fisheries showed good fit to observed length frequencies, with matching distributions shapes (low NRMSE) and low mean length bias (low SMD; Figure 6). The model showed a poorer fit to length distributions from fisheries S6 and O15, as expected given the poor data quality associated to these fisheries (cf Appendix Table 4). When using independent datasets, the fit to length frequencies deteriorated for some of the fisheries, and particularly for the pre-MLE period (1983-1998). This may be linked to the parameterization of fisheries selectivities parameters, which were not estimated in the MLE (cf Section 2.2.3). The estimation of model parameters in the MLE may have been constrained by the selectivity values chosen *a priori*, so model prediction may be

pertinent for the MLE period and the short independent post-MLE 2019-2022 period, but less so for the longer pre-MLE 1983-1998 period.

Length frequencies fit metrics are summed up in Table 1, where a weighted average of fisheries-sepcific NRMSE and SMD were computed, using proportions of total sample counts as weights.

3.2.3 Tag fit metrics

The model showed good fit to tag recaptures, reproducing the longitudinal and latitudinal profiles of recaptures with accuracy (Figure 7). Yet, this is expected for a relatively resident species such as the yellowfin tuna (cf next Section 3.4.4), with recaptures close to tag releases. Still, the model predicted slightly more diffusion of tag densities than observed, notably around tag released in the North East of the EPO basin. Remarkably, even better fit metrics were obtained when using the independent validation dataset.

(a) MLE dataset - 1999-2018

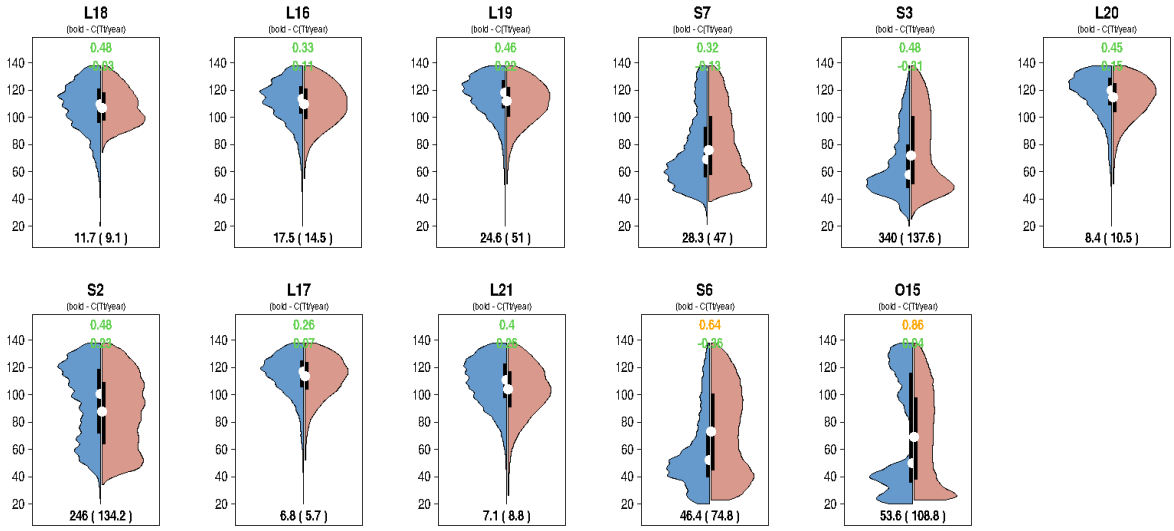

(b) Validation dataset - 1983-1998

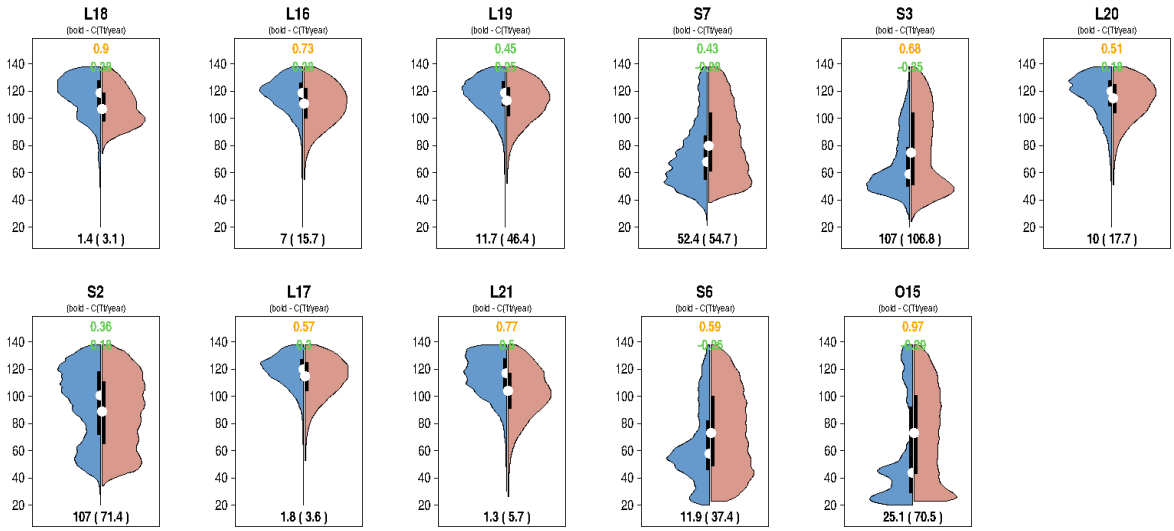

Figure 6: Fisheries-specific length frequencies fit metrics.
continued...

Figure 6 continued

(c) Validation dataset - 2019-2022

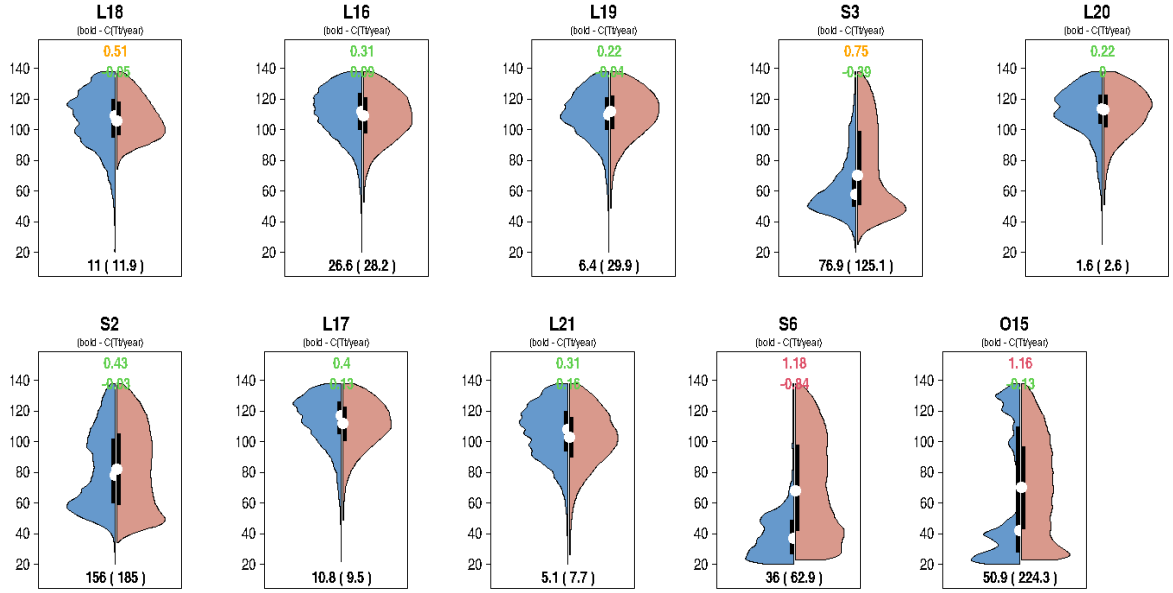

Figure 6: Fisheries-specific length frequencies fit metrics. In each fishery-specific panel, observed (blue) and predicted (red) length frequencies are displayed. The difference in observed and predicted frequencies shapes is measured with NRMSE and displayed on the first top row, while the bias between observed and predicted mean length are displayed in the second top row. Scores are represented with green, yellow and red colors when the metric is deemed good, fair or bad. Only fisheries that represent >1% of total samples are displayed here.

(a) MLE dataset

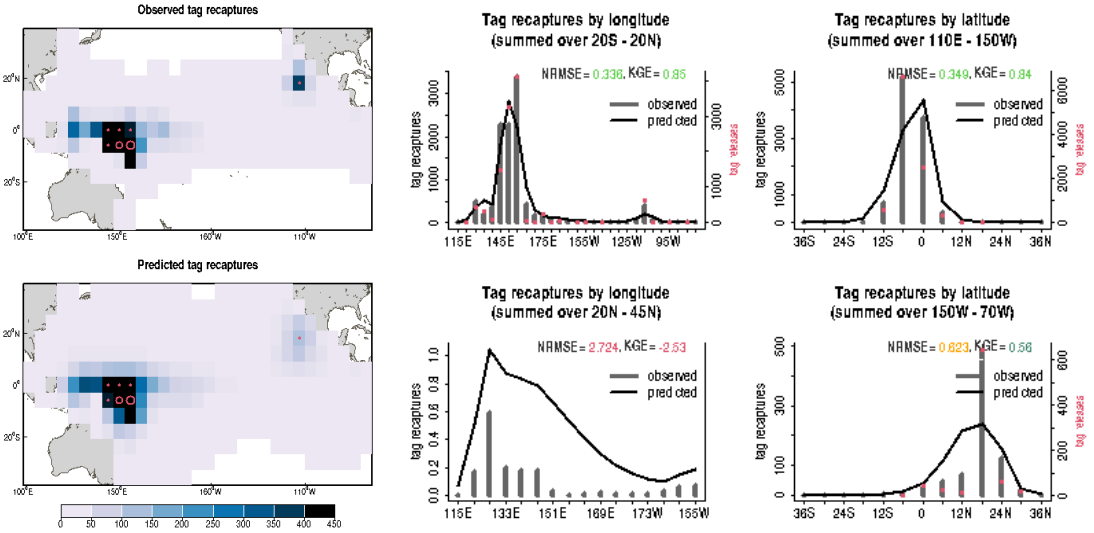

(b) Validation dataset

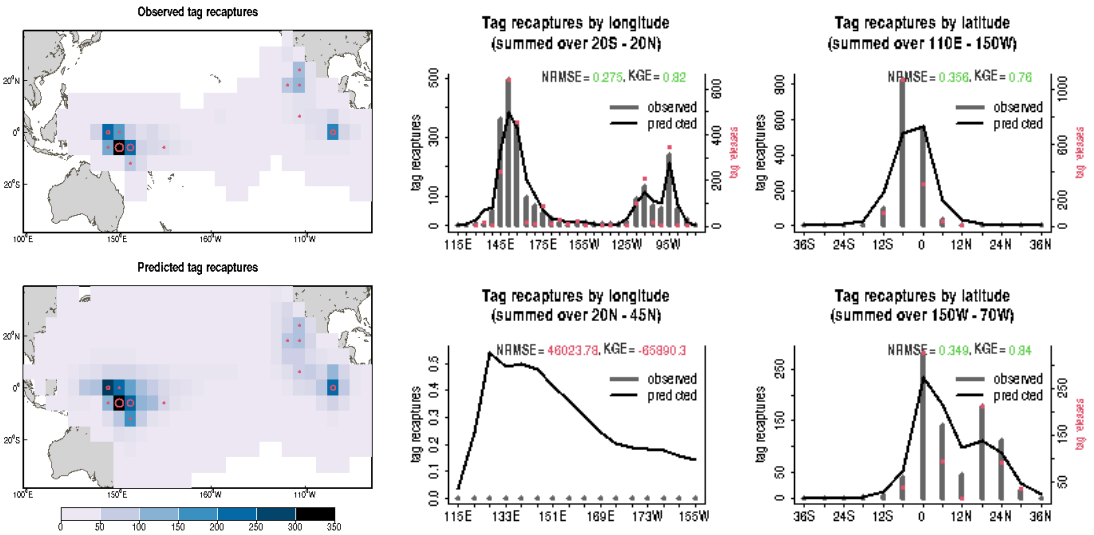

Figure 7: Observed vs predicted tag recaptures. Maps of observed and predicted tag recaptures are displayed for the MLE and the validation dataset on left panels. Longitudinal profiles of observed (grey bars) and predicted (black line) tag recaptures are displayed in the central panels, extracted on the 20°S-20°N band (Note: the longitudinal profiles extracted on the 20°N-45°N band are irrelevant as nearly no tag recaptures were observed nor predicted in that band). Tag releases are represented with red dots. Latitudinal profiles of tag recaptures in the WCPO and EPO are displayed in the left panels. Divergence between observed and predicted profiles shapes is quantified with NRMSE and KGE metrics, with color coding representing good (green), fair (yellow) and bad (red) fit.

3.2.4 Larval fit metrics

Seasonal variability of input Larval Density Index (cf Section 2.4.3) was fairly reproduced in most of the regions with high larval density (regions 3 to 6; Figure 8), with predicted larval density showing relatively high correlation to seasonal profiles (Pearson R from 0.7 to 0.97). A noticeable exception is the region R1, encompassing the Kuroshio region, where the model failed to reproduce the strong seasonal pattern of LDI, characterized

by a significant increase during the boreal spring. Observed LDI and predicted larval density showed close distributions across environmental variables (Figure 8), except for SST.

The model predicted larval densities distributed over a wider range of SST, notably towards colder temperatures, than in the input larval data, characterized by a sharper decline under 30°C. This may indicate a failure of the present model configuration to describe the biological processes involved in larvae dynamics. Indeed, in the current configuration, larvae are the output of stock-recruitment multiplied by spawning habitat index H_s. The early-larvae model configuration used in Senina et al. (2025), that includes a specific temperature-dependent hatching success rate, and that distinguishes between the first few days of life, with mortality independent of prey availability, and the later days, with regular H_s-dependent mortality, may be more appropriate in that regard.

This divergence should be interpreted with caution, however, because the input LDI is not based on direct observations but rather on the output of a geostatistical model fitted to larval presence–absence data (cf Section 2.4.3), and is therefore itself subject to prediction error.

(a) Regional seasonal patterns

(b) Distribution across env. variables

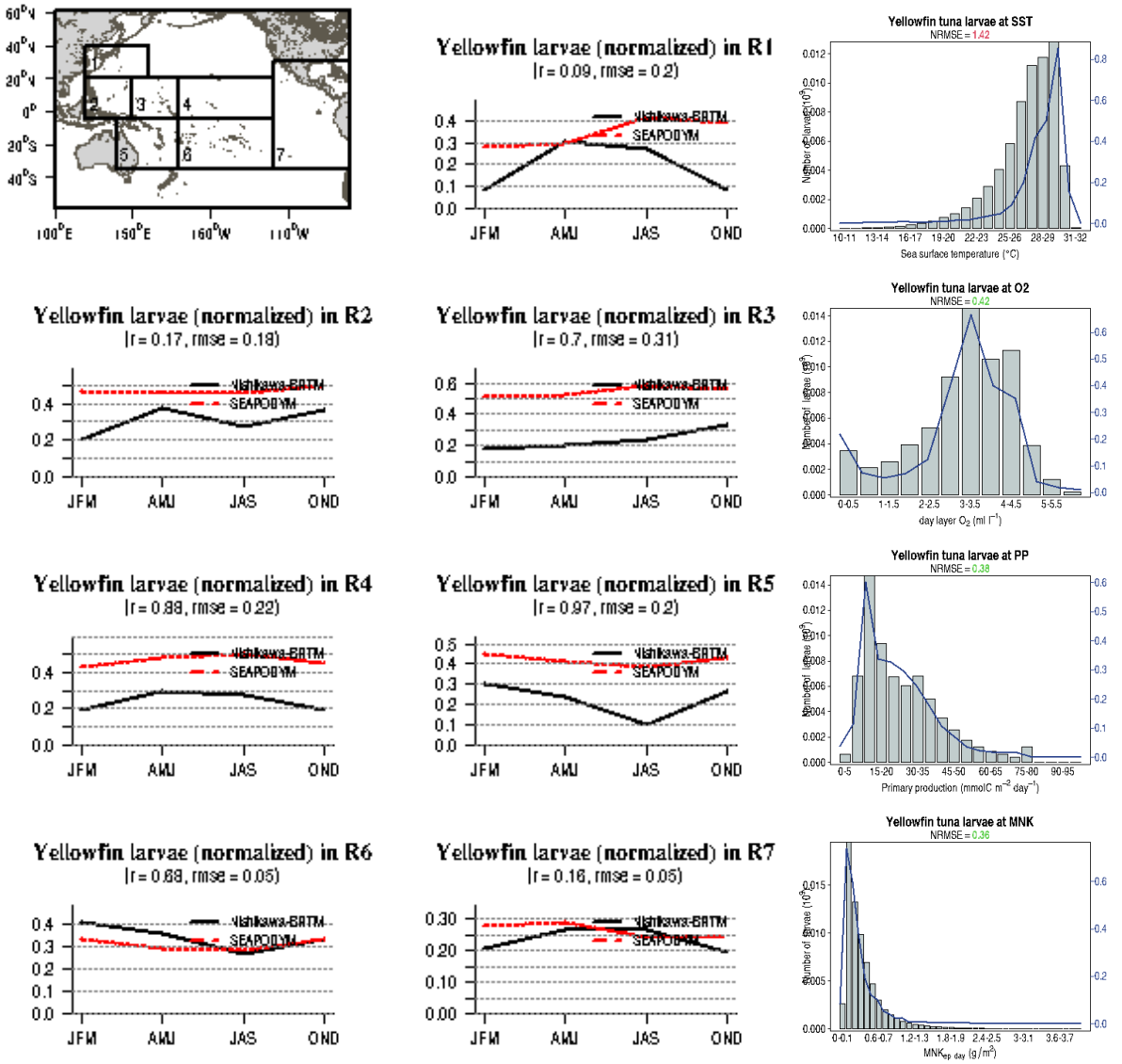

Figure 8: Larval Density Index vs predicted larvae density - Seasonal and environmental profiles. a) Seasonal profiles of LDI and predicted larvae density were extracted on rectangular regions, Pearson R and NRMSE were computed to assess statistical fit. b) The distribution of LDI and predicted larvae density across Sea Surface Temperature (SST), dissolved Oxygen (O2), Primary Production (PP; proxy for larval prey density) and epipelagic micronekton (MNK; proxy for larvae predator density) were compared and NRMSE was computed to assess statistical fit.

3.3 Comparison to previous reference model

Spatial distributions and diagnostics of statistical fit to the different observation datasets were compared to the previous INTERIM reference solution (Senina et al. 2019) and are provided in Senina et al. (2026a). From this comparative study, the present model solution emerges as an improvement over the previous reference model, providing a more realistic representation of spatial distributions and a better fit to catch-effort data. The fit to tagging data however deteriorated in the present model solution. This underlines

the need for future work to notably focus on reaching a proper MLE including movement parameters. Indeed, as indicated in Section 3.1, the present model solution consist in a hybrid MLE where movement parameters were corrected from a separate solution.

3.4 Best model parameters

SEAPODYM model parameters associated with the best solution reached during the calibration work (cf Section 3.1) are available in Appendix Table 3.

3.4.1 Spawning habitat and reproduction

A new thermal function for the spawning habitat was implemented, allowing a double logistic threshold shape. The estimated thermal function showed maximal suitability over a large range of SST values, with no upper limit and a slowly decreasing suitability for temperatures <22°C (Figure 9). Indeed, the upper temperature threshold was estimated at its upper bound, 32°C, which is nearly out of the observed SST range (first and 99th percentile = 1.4 and 30.2 °C respectively). The spawning habitat shows strong dependency to prey density in low prey density areas, with decreasing suitability with decreasing prey density, but weaker dependency in high prey density area (flat relationship observed over $0.5 g.m^{-2}$). Larvae predator density has a lower impact than prey density on spawning habitat, with a relatively flat relationship over most of the predator density range of values ($\sim$0.2-4$g.m^{-2}$), with highest suitability in very low predator density areas.

The estimated stock-recruitment showed a strongly non-linear shape, with a steep increase when spawning density $<0.5 km^{-2}$ (i.e. 10th percentile of spawning density values), and a plateau reached around $1 km^{-2}$ (i.e. 23rd percentile of spawning density values). The absolute value of this plateau cannot be interpreted directly though, as stock-recruitment is highly correlated to other model parameters, such as the ones involved in mortality (and notably fishery selectivity parameters, which were not estimated in the MLE).

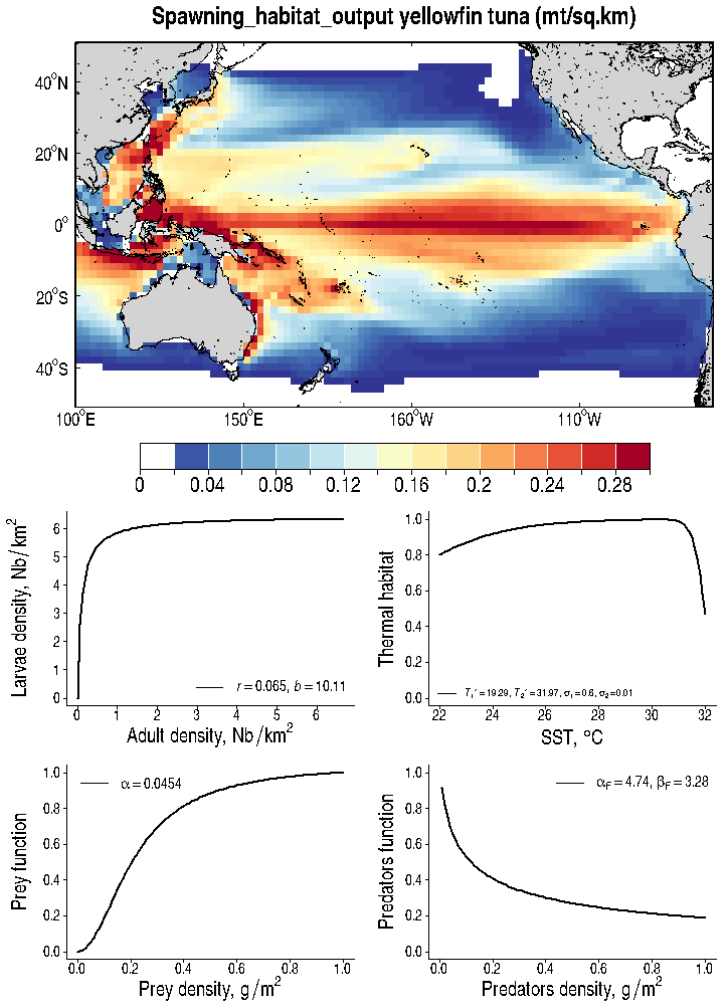

Figure 9: Spawning habitat and stock recruitment relationship.

3.4.2 Natural mortality

Natural mortality rates must be considered with caution as they are highly correlated to reproduction and fisheries selectivity. Here, this is especially true given that fisheries selectivity were not estimated within the MLE, but fixed to values defined using observed global length frequencies. Nonetheless, natural mortality rates were estimated at $5.7yr^{-1}$ (including environment-dependent mortality) for the first monthly age class, with a fast decline during the first year of life ($0.19yr^{-1}$ at $12mo$), a minimum of $0.15yr^{-1}$ reached at $14mo$, then a slow linear increase due to senescence, reaching $0.81yr^{-1}$ for the A+ class ($>82mo$).

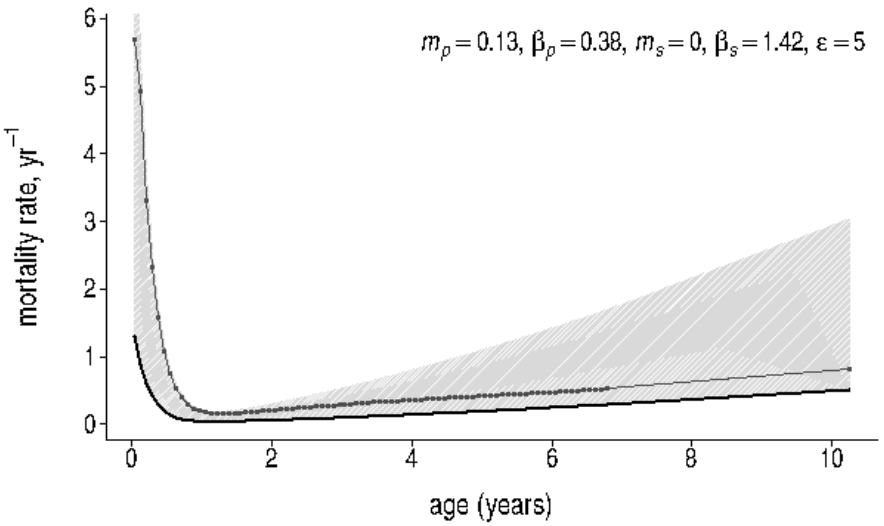

Figure 10: Natural mortality at age. The black line represent the baseline theoretical mortality-at-age function. The grey shaded area represents the theoretical range of habitat-dependent mortality rates, when habitat index varies between 0 and 1. Black dots represent the realized mortality rates, considering the distribution of tuna densities across habitat index values.

3.4.3 Feeding habitats

Optimal temperature decreases with age following a non linear trend, from 29.2°C for the youngest age classes to 26.6°C for the oldest age class (Figure 11). The thermal range around the optimum is low for youngest age classes (∼1.05°C) and high for oldest age classes (∼4.5°C).

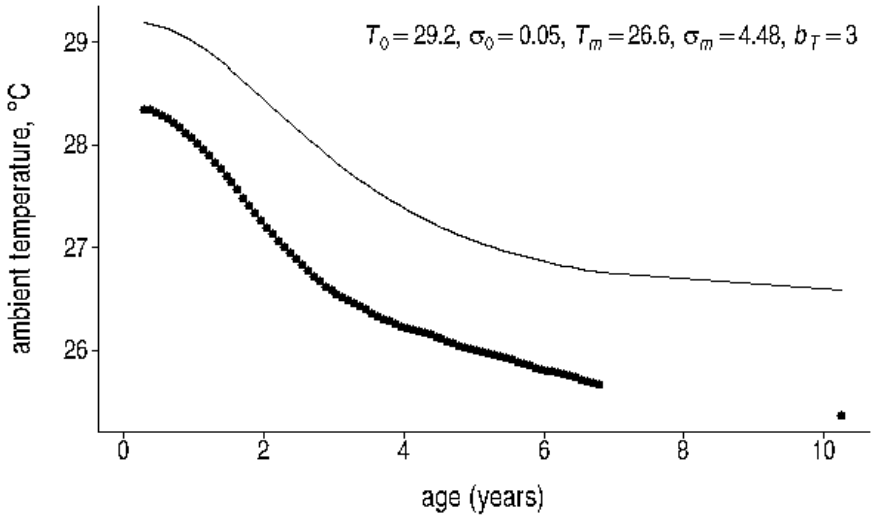

Figure 11: Age-dependent thermal accessibility. The black line represent the baseline theoretical thermal accessibility function. Black dots represent the mean ambient temperature experienced by tunas, considering the distribution of tuna densities across ambient temperature values (SST for larvae, epipelagic temperature for small juveniles, and a weighted average of layers temperature for juveniles and adults).

The use of a corrected field for epipelagic layer temperature, that brings temperature closer to SST in areas with strong vertical thermal gradient, allowed to better describe the species environment, and thus resulted in a significant improvement of the model solution. Indeed, this aligns with knowledge on this species behavioural ecology, which has been shown to use more superficial layers in areas with lower mixed layer depth (Schaefer et al. 2007). The use of this temperature field notably enabled to better describe the high catch observed in the EPO, in regions where the original temperature field described a cold habitat, inconsistent with the thermal preference estimated in the western and central pacific (cf Section 3.1 and Appendix Figure 23).

Data from archival tagging were analyzed in comparison to the thermal habitat predicted by the model and exhibited good qualitative agreement. Mean model temperature (i.e. layer temperature weighted by tuna density and by layer contribution to feeding habitat) displayed the same decreasing trend with age as daily mean observed temperature from archival tag data, but 1 to 1.5°C warmer (Figure 12). SEAPODYM thermal preference in two age groups were extracted and weighted with the same age-distribution as archival tag data to enable a comparison free from sampling bias. The comparison showed some agreement for young tunas (here $<40mo$), with a similar temperature mode for SEAPODYM and archival tag (27.3 and 27°C), but with a much wider range of temperatures in archival tag data. For the older group ($>40mo$), the temperature range matched with archival tag data, but with a warmer temperature mode in the SEAPODYM predictions (26.1°C) than in the archival tag data (24.7°C).

Indeed, for the older age group, archival tag data showed a slightly left-skewed distribution while SEAPODYM preidctions showed a slightly right-skewed distribution. This initially led to re-consider our model configuration, that models theoretical thermal accessibility as a symetrical gaussian, to a new configuration allowing asymetry. Optimization runs with this new configuration resulted in the same symetrical thermal function as the baseline configuration. The baseline configuration with symetric thermal function was thus selected for simplicity.

(a) Mean temperature vs. age

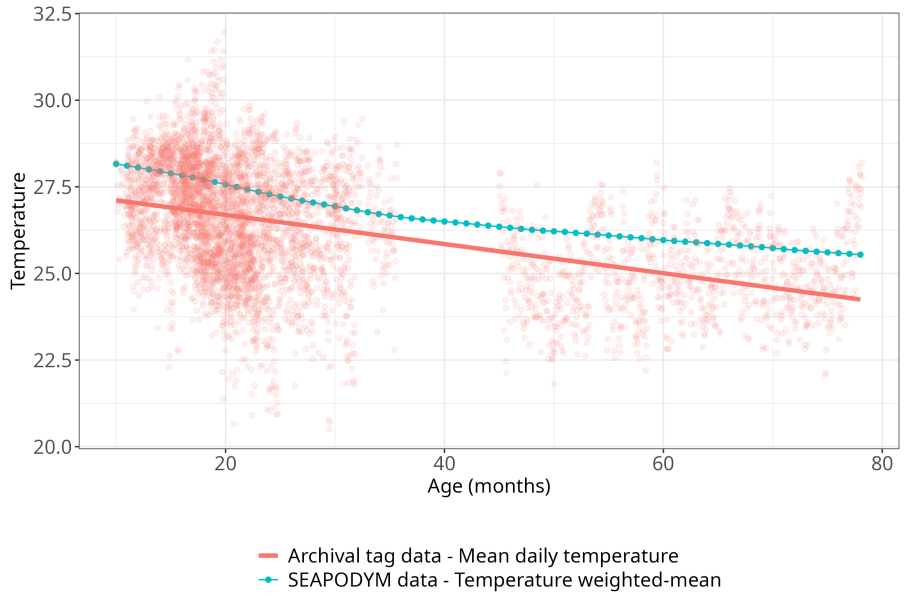

(b) Temperature distributions in two age groups

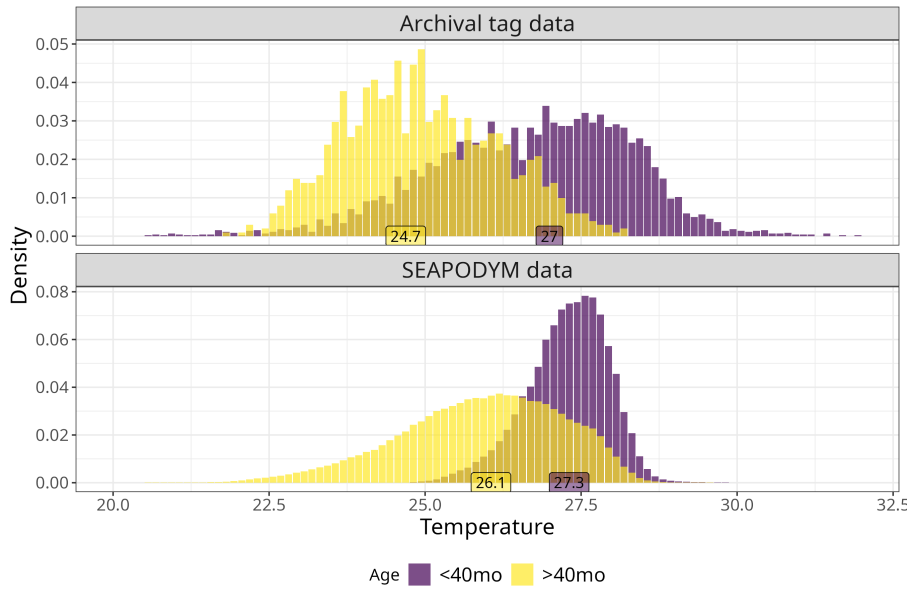

Figure 12: Comparison to age-dependent thermal habitat from archival tag data. a) Daily mean temperature from archival tag data are displayed in red, with a red line showing the linear trend with age. Average temperature was computed as an average of the 3 layers' temperature, weighted by their contribution to feeding habitat, and weighted by tuna density. The weighted average per age class is displayed in blue. b) Based on age distribution of archival tag data, two age group were identified: younger and older than 40*mo*. Distribution of daily tag temperatures and SEAPODYM average temperature (weighted layer contribution to feeding habitat and by tuna density) were extracted for each group.

Spatially, feeding habitats differ between young and old age classes. Best habitats for young tunas are concentrated in the equatorial zone, in the Indo-Pacific region, the western and central pacific and a concentrated area along the coast of Americas between southern Mexico and Costa Rica (Figure 13). As tuna age, feeding habitats extend

eastward in the Pacific tropical zone, and towards higher latitudes, with pockets of high quality habitats to the south-east of Japan, in the China sea, and the Coral sea. Low habitat quality observed right on the equator can be explained by low forage density in the epipelagic layer, washed away from the equator by the strong eastward equatorial current (Appendix Figure 26 and 27).

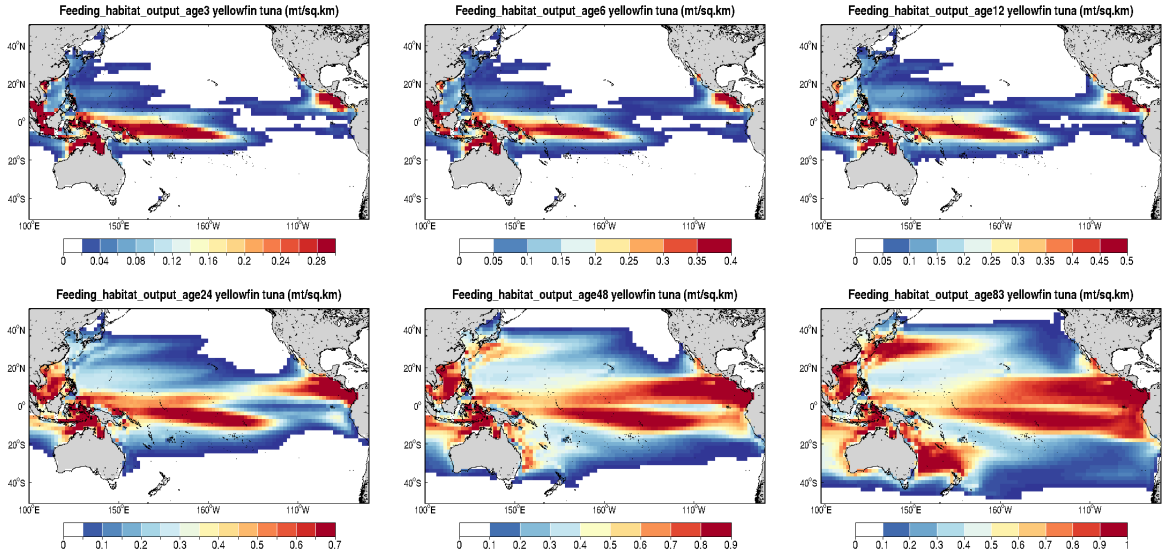

Figure 13: Age-dependent feeding habitat. Feeding habitat was averaged over the 2009-2018 decade for the age classes $3mo$, $6mo$, $12mo$, $24mo$, $48mo$ and the A+ class.

The feeding habitat is mostly driven by the epipelagic forage, with this layer contributing to >90% of the feeding habitat in the equatorial region (Figure 14 and Appendix Figure 28). This may be a misrepresentation of the species biology as the yellowfin tuna is known to forage in the upper mesopelagic layer and is caught by longline fisheries at these depths. Still, for older age classes here, the upper mesopelagic layer forage can contribute to 30 to 50% of the feeding habitat in higher latitudes, notably in the pockets of habitats in the Coral Sea and South-East of Japan.

(a) Feeding habitat index

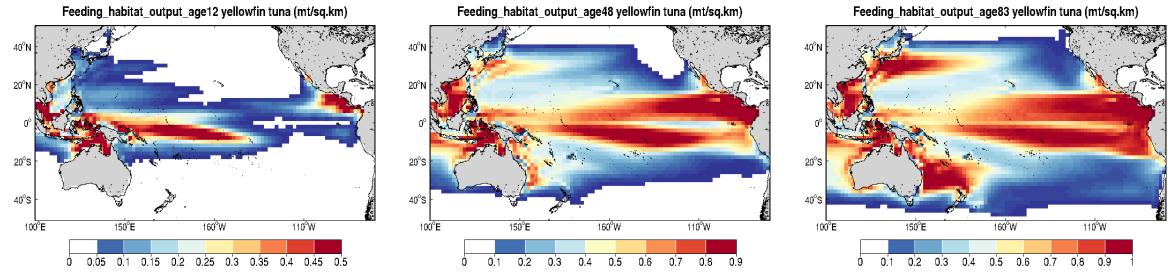

(b) Layer contribution to feeding habitat index

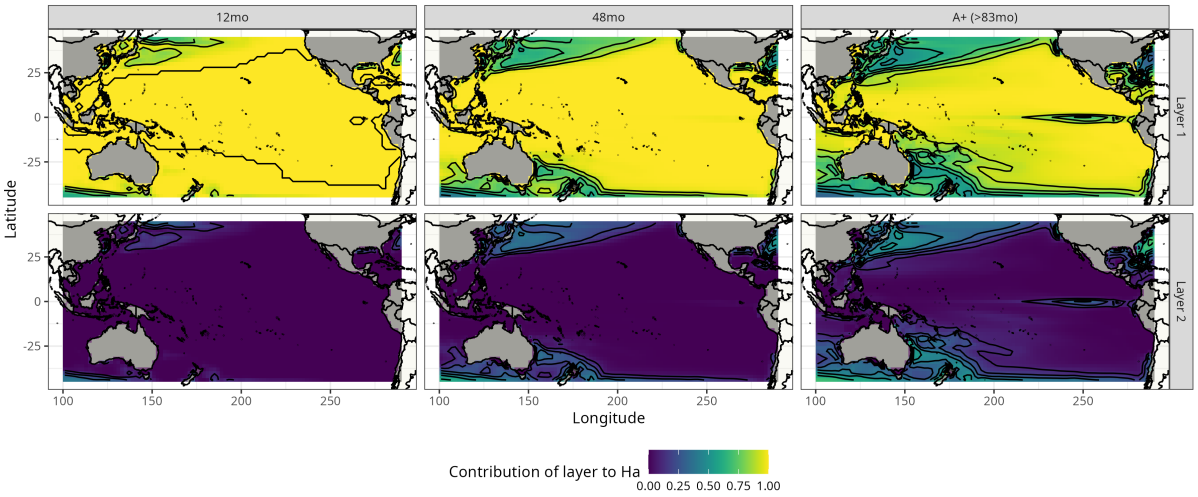

Figure 14: Contribution of vertical layers to feeding habitat. For each age class, the contribution of each of the three vertical layers to the feeding habitat index can be computed as the proportion of accessible forage in the layer. Here, only layer 1 (epipelagic layer) and 2 (upper mesopelagic) are displayed, as the lower mesopelagic layer does not contribute to feeding habitat.

The disproportionate contribution of the epipelagic forage to feeding habitat prevented from accurate estimation of the oxygen accessibility function across the entire range of oxygen values. Indeed, the response to low oxygen concentration could not be observed from data, as the epipelagic layer is characterized by high concentration of oxygen over the entire spatial range ($>4mL.L^{-1}$), and similarly for the upper mesopelagic layer, with oxygen concentrations that remain high in regions with higher contribution to feeding habitat. (Figure 14). The oxygen parameters were thus set to physiological values from literature (Brill 1994) and not estimated in the MLE.

3.4.4 Movements

Horizontal density speeds associated to advective movements decrease with age (Figure 15), with rates of directed movements higher in young age classes, which mostly drift with ocean currents, than in older age classes, which are able to swim faster than currents and escape strong current systems by diving to deeper layers. At the opposite, rates of

diffusive movements increase with age, which is indicative of improved abilities to swim away from bad quality habitats.

The movements patterns can be characterized as advective for the yougest age classes, with a Peclet number of 3.75 for the first mobile age class (age = $3mo$), and as diffusive for the oldest age classes, with a Peclet number of 0.57 for the A+ age class.

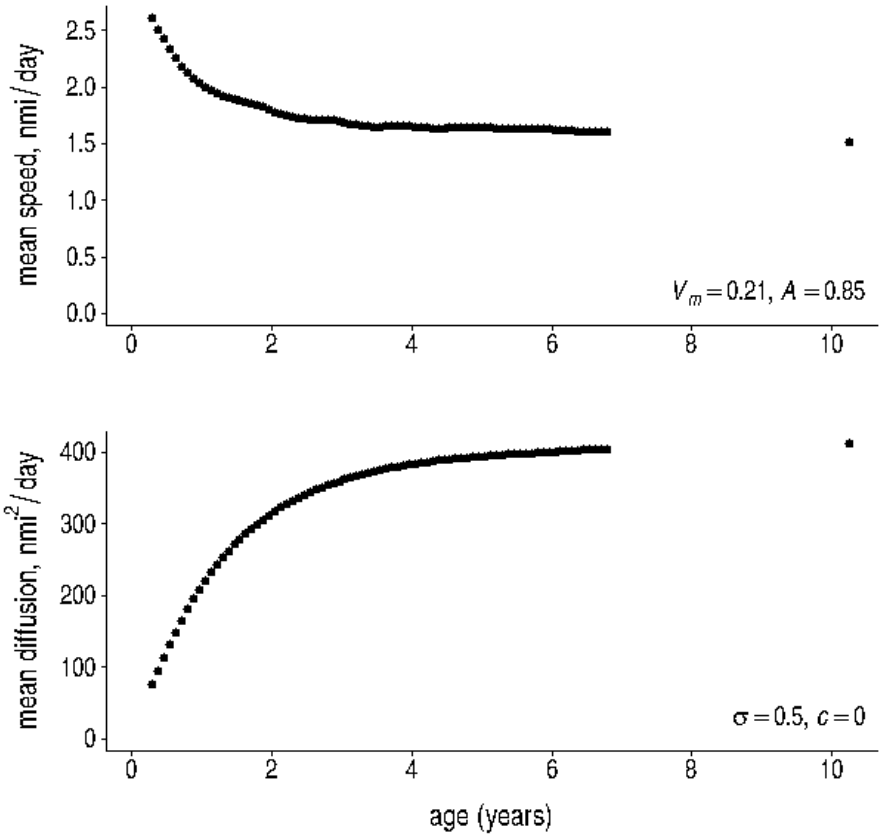

Figure 15: Movement rates. Movement rates are computed as weighted averages over the temporal and spatial scale, using tuna density as weight.

Rates of horizontal directed movements in adults are low compared to other tropical tuna species (Senina et al. (2025) for skipjack tuna and Senina et al. (2026a) for bigeye tuna), which is consistent with the higher residensy and lower long range movement patterns observed in this species (Fonteneau 2014; Fonteneau 2008).

3.4.5 Fisheries parameters

Effort-based catch predictions were used for 13 out of the 22 fisheries, for which catchabilities were estimated. Linear trends in catchabilities, designed to account for the development of fishing technologies, were allowed and estimated as well. Estimated values of catchabilities and their slope across time are available in Table 3. For most of these fisheries, residual errors between overall catch predictions and observations were low and with no trend in time, indicating the catchabilities and their slope were correctly estimated (Appendix Figures 29 and 30). Catchabilities of P12 and P13 may have been

under-estimated, as the optimization process reached their upper bound. Their predicted catch was thus systematically lower than observed catch. This issue is yet not likely to have any consequences over the MLE or model predictions, as these fisheries respectively represent 0.002 and 0.2% of total catch. The catchability of the P14 fishery was also estimated at its upper bound, but very low residual errors were observed for this fishery, with even slightly higher higher predicted than observed catch.

Selectivity parameters were not included in the optimization process and were set to *a priori* values consistent with overall length frequencies. Future work will focus on estimating these parameters along with biological parameters, which may impact the model solution, notably the parameters associated to recruitment and mortality, and may in time improve the model predictive skills on recuitment and stock level.

3.5 Spatial and temporal dynamics

Model development is still in progress, notably on the inclusion of selectivity parameters in the MLE. Model predictions about stock and recruitment level should thus be taken with caution. Consequently, we will focus in this section on the spatial and temporal dynamics of fish densities, rather than their absolute values and the impact of fishing pressure.

3.5.1 Spatial distribution

The spatial distribution of larvae closely matches the spawning habitat (Figures 16 and 9), with little dependence on spawner density because the stock–recruitment relationship reaches an asymptote at relatively low levels of spawning biomass.

Mortality and movement processes drove older age classes to diverge from the larvae distribution, resulting in a more contrasted pattern of adult biomass, concentrated in a tropical band and in distinct hotspots at higher latitudes, particularly in the Kuroshio region of the North Pacific and along the East Australian current in the Coral Sea. More precisely, within the tropical band, a WCPO hotspot extends eastward on either side of the equator, forming northern and southern branches. The northern branch stretches across the Pacific and connects to a secondary hotspot located along the eastern Pacific coast between southern Mexico and Costa Rica.

Total biomass distribution broadly matches total observed catch spatially, except in a few localized areas, notably North of 20°N along the eastern Pacific coast or in the Indo-Pacific region surrounding the Indonesian and Philippine archipelagos. In the latter region, this discrepancy may be related to the difficulty of physical and biogeochemical ocean models in accurately representing the highly complex environmental conditions associated to intricate coastlines, narrow straits, and rugged bathymetry. These limitations are likely further exacerbated by the coarsening of environmental fields to a 2x2° grid here, which reduces the ability to resolve circulation patterns and habitat heterogeneity within archipelagic waters.

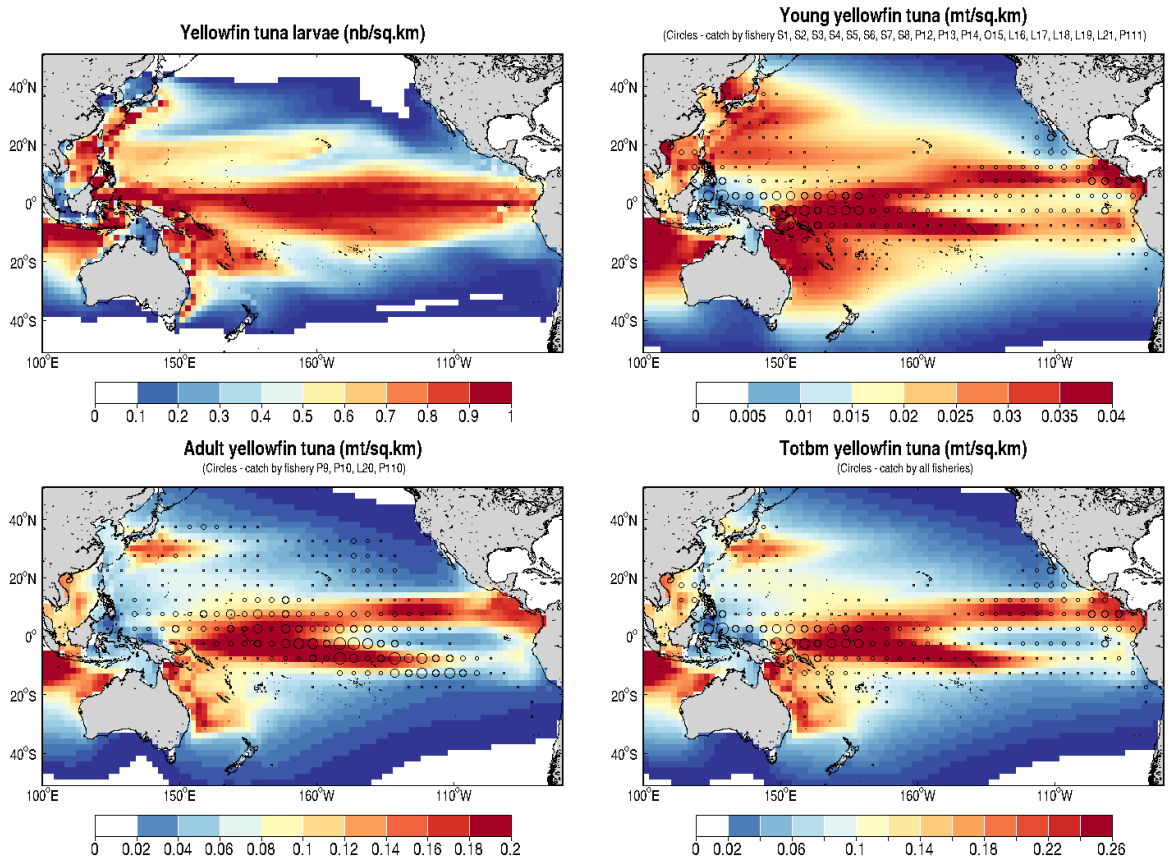

Figure 16: Spatial distribution of population density for different life stages. Black circles represent observed catch, with fisheries segregated as mostly targetting juvenile tunas (referred to as 'young' on the maps), no targetting of juvenile tunas or all combined. Note that this segregation of fisheries can mask the fact that adults can also be caught by "juvenile targetting" fisheries.

3.5.2 Environmental variability

The impact of environmental variability on biomass distribution was assessed using predictions from simulation without fishing pressure.

Longitudinal oscillations of equatorial biomass can be observed from model predictions, a likely response to zonal shifts of the warm pool related to El Niño Southern Oscillation (ENSO). Such pattern is particularly visible in the southern equatorial region, where the center of gravity (COG) of total biomass shows strong negative correlation to Southern Oscillation Index (Pearson R^2 = -0.66; Figure 17), corresponding to eastward shift during El Niño regime.

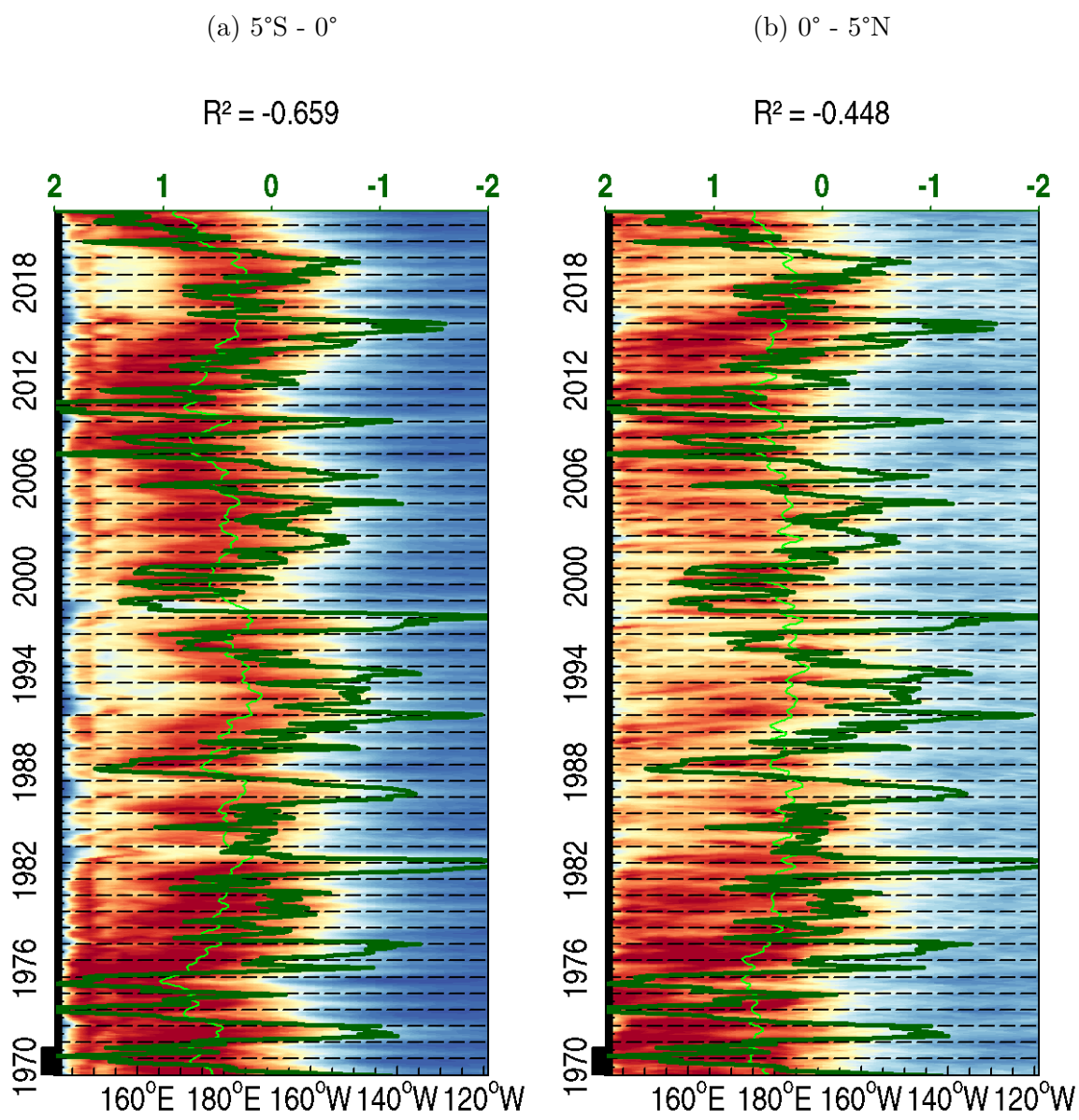

Figure 17: Zonal oscillations of biomass COG as a response to ENSO. Center of gravity (COG) of total biomass (light green line) were extracted in a southern and northern equatorial band. A linear model was built to assess correlation with SOI (dark green line), a climate index indicative of ENSO, that shows positive values for La Niña regime and negative values for El Niño regime.

Over the 1974-2022 period, simulations showed an eastward shift of total biomass in the equatorial band (5°S-5°N), a likely response to the shift of the warm pool (Figure 18). The poleward shift of biomass in the northern part of the WCPO may be a response to warming and extension of thermal suitability towards higher latitudes (cf Appendix Figure 32). Southern WCPO biomass did not show such a trend, while EPO biomass showed an opposite trend, with a slight shift towards the equator.

(a) Longitudinal shift of biomass

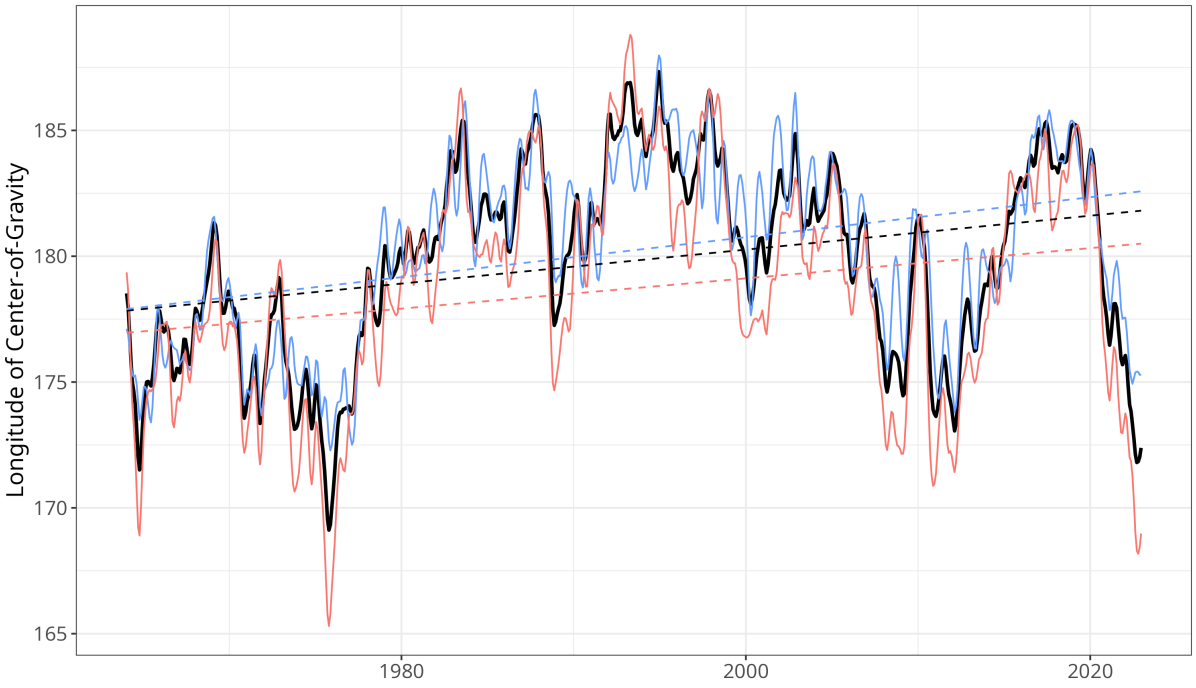

(b) Latitudinal shift of biomass

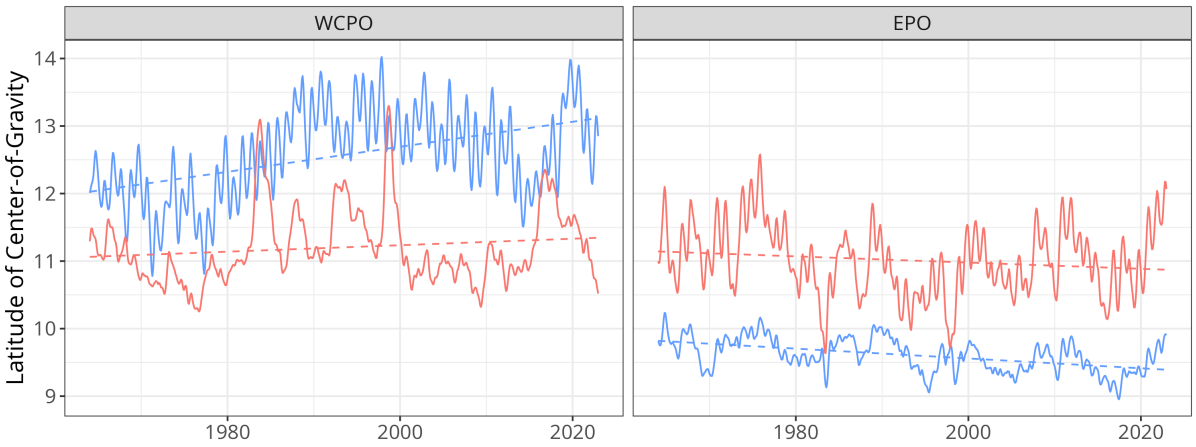

Figure 18: Longitudinal and latitudinal shift of biomass. a) Longitudinal center ofgravity of total biomass was extracted in an equatorial band between 5°S and 5°N to display eastward shift of biomass, with northern and southern subsets respectively displayed with blue and red. b) Latitudinal center of gravity of total biomass was extracted between 0 and 40°N (blue) and between 0 and 40°S (red), in the WCPO and EPO regions.

3.5.3 Recruitment

As explained above, absolute levels of recruitment are subject to caution, and thus only spatial and temporal patterns of recruitment can be interpreted. For comparison with predictions from the MFCL stock assessment model, recruitment was extracted in the same rectangular regions and the relative contribution of these regions to overall recruitment was computed (Figure 19). In the WCPO, most of the recruitment occurs in the

region R4 (31% in the WCPO, 21% overall), followed by region R1 (27% WCPO, 18% overall) then R5 (24% WCPO, 16% overall). At the basin scale, the WCPO contributes twice as much as the EPO to total recruitment (67% vs. 33%).

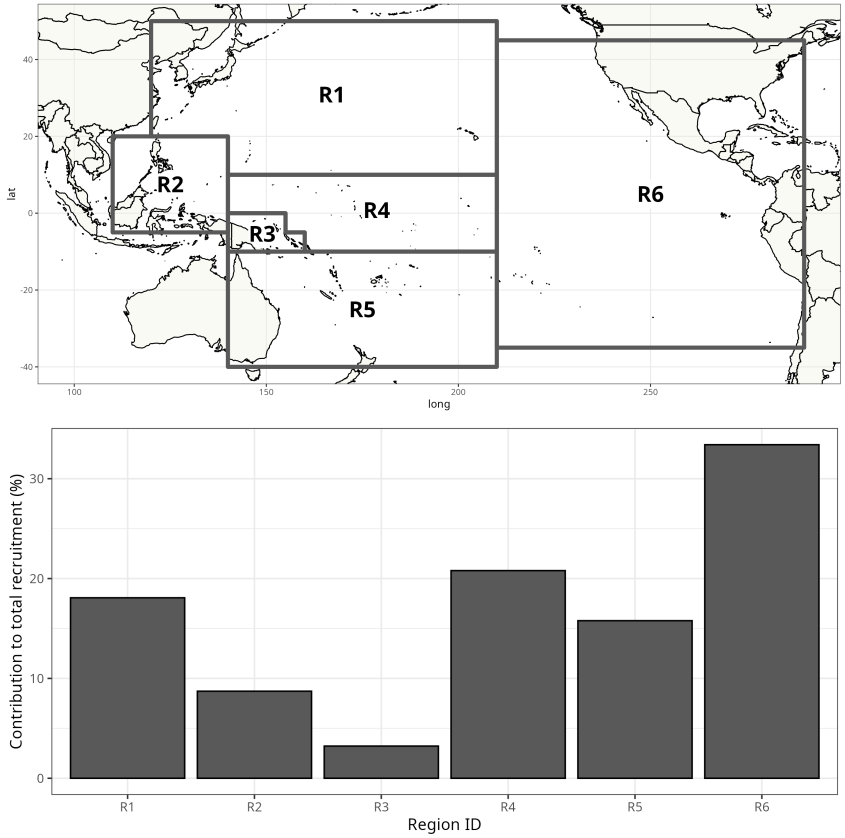

Figure 19: Contribution of regions to recruitment in the Pacific Ocean. Regions R1 to R5 follow the same definition as the regions used in the MULTIFAN-CL stock-assessment, while R6 represent the EPO region.

4 Discussion

The solution presented here represents a substantial improvement over the previous reference model, providing a more realistic description of spatial distributions and a better fit to the catch-effort data. These advances indicate significant progress in model performance and predictive capability. However, this solution should not yet be regarded as a final reference model, as it does not correspond to a fully consistent MLE. In particular, the movement parameters were manually adjusted rather than estimated within the optimization framework, and selectivity parameters were not jointly estimated with the biological parameters. As a consequence, we do not deem model predictions of absolute values of tuna biomass as reliable and cannot therefore bring estimates of tuna stock, nor assess the impact of fishing pressure.

Still, the progress made along model development brought a better understanding of the final model configuration, notably concerning the choice of shapes of functional

responses to the environment, the description of the environment, the configuration of individual fisheries, and the impact of different data types on MLE solution.

The solution presented here appears to be particularly well fitted to model juveniles and young adults, with a model characterized by a high contribution of the epipelagic layer to feeding habitat, a high habitat-dependent mortality and a good fit to data from fisheries targetting those stages (mostly purse-seine data). Next steps of model development will focus on providing a better representation of adult behaviour, with improvements to both the description of feeding habitat and the modelling of movement patterns.

Once a final reference model is reached, future steps will consist in using an ensemble of Earth System Model ocean forcings to investigate the impact of future climate change, and provide future projections of tuna stock and distributions, for various Shared Socio-economic Pathways and up to the horizon 2080.

5 Declaration of AI-assisted technologies usage

Generative AI tools (ChatGPT, Claude, Copilot) were used to assist with code development and text redaction. All analytical choices, model specifications, diagnostic interpretations, and conclusions are those of the authors, who reviewed and verified all AI-assisted output. The methodology, model implementation, and the scientific conclusions are the responsibility of the authors.

6 References

References

Brill, Richard W. (1994). "A review of temperature and oxygen tolerance studies of tunas pertinent to fisheries oceanography, movement models and stock assessments". en. In: *Fisheries Oceanography* 3.3. _eprint: https://onlinelibrary.wiley.com/doi/pdf/10.1111/j.1365-2419.1994.tb00098.x, pp. 204–216. ISSN: 1365-2419. DOI: 10.1111/j.1365-2419.1994.tb00098.x. URL: https://onlinelibrary.wiley.com/doi/abs/10.1111/j.1365-2419.1994.tb00098.x (visited on 12/19/2023).

Schaefer, Kurt M., Daniel W. Fuller, and Barbara A. Block (Sept. 1, 2007). "Movements, behavior, and habitat utilization of yellowfin tuna (Thunnus albacares) in the northeastern Pacific Ocean, ascertained through archival tag data". In: *Marine Biology* 152.3, pp. 503–525. ISSN: 1432-1793. DOI: 10.1007/s00227-007-0689-x. URL: https://doi.org/10.1007/s00227-007-0689-x (visited on 07/06/2026).

Fonteneau, Alain (2008). *Tuna movement patterns presently shown in the Indian Ocean by tag recoveries*.

— (2014). "Fifty years of dart tag recoveries for tropical tuna: A global comparison of results for the western Pacific, eastern Pacific, Atlantic, and Indian Oceans". In.

Kobayashi, Shinya, Yukinari Ota, Yayoi Harada, Ayataka Ebita, Masami Moriya, Hirokatsu Onoda, Kazutoshi Onogi, Hirotaka Kamahori, Chiaki Kobayashi, Hirokazu Endo, Kengo Miyaoka, and Kiyotoshi Takahashi (2015). "The JRA-55 Reanalysis: General Specifications and Basic Characteristics". In: *Journal of the Meteorological Society of Japan. Ser. II* 93.1, pp. 5–48. DOI: 10.2151/jmsj.2015-001.

OFP-SPC (2019). *Project 90 Update : Better data on fish weights and lengths for scientific analyses — WCPFC Meetings*. Working Paper WCPFC-SC15-2019/ST WP-03. Pohnpei, Federated States of Micronesia: WCPFC. URL: https://meetings.wcpfc.int/node/11219 (visited on 07/04/2026).

Senina, Inna, John Hampton, Lucas Bonnin, Patrick Lehodey, Paul Hamer, and Simon Nicol (2019). *Spatial structure and regional connectivity of bigeye and yellowfin tuna stocks in the WCPO derived from the reference SEAPODYM models — WCPFC Meetings*. Information Paper. 19th Regular Session of the Scientific Committee. URL: https://meetings.wcpfc.int/node/19371 (visited on 07/16/2024).

Senina, Inna N., Patrick Lehodey, John Hampton, and John Sibert (May 2020). "Quantitative modelling of the spatial dynamics of South Pacific and Atlantic albacore tuna populations". en. In: *Deep Sea Research Part II: Topical Studies in Oceanography*. Oceanic biodiversity under climate change: shifts in natural and human systems 175, p. 104667. ISSN: 0967-0645. DOI: 10.1016/j.dsr2.2019.104667. URL: https://www.sciencedirect.com/science/article/pii/S0967064519301511 (visited on 07/05/2023).

Buenafe, Kristine Camille V., Jason D. Everett, Daniel C. Dunn, James Mercer, Iain M. Suthers, Hayden T. Schilling, Charles Hinchliffe, Alvise Dabalà, and Anthony J. Richardson (July 2022). "A global, historical database of tuna, billfish, and saury larval distributions". en. In: *Scientific Data* 9.1, p. 423. ISSN: 2052-4463. DOI: 10.

1038/s41597-022-01528-7. URL: https://www.nature.com/articles/s41597-022-01528-7 (visited on 08/16/2023).

Senina, Inna, Olivier Titaud, Guillaume Briand, and Patrick Lehodey (2022). *SEAPODYM: spatial ecosystem and population dynamics model for migratory age-structured stocks [version 4.0]*. Reference Manual. URL: https://purl.org/spc/digilib/doc/vxsz3.

Magnusson, Arni, T Teears, John Hampton, C Castillo Jorda, Tom Peatman, Robert Scott, Finlay Scott, Nan Yao, Graham Pilling, and Paul Hamer (2023). *Stock assessment of yellowfin tuna in the Western and Central Pacific Ocean: 2023 (7Aug2023) - Final (Rev.02 on 15Sep2023) — WCPFC Meetings*. WCPFC. URL: https://meetings.wcpfc.int/node/19352 (visited on 12/17/2024).

OFP-SPC (2025). *Tuna fishery yearbook 2025*. WCPFC.

Senina, Inna, Lucas Bonnin, Hidetada Kiyofuji, Kristine Camille V. Buenafe, John Hampton, Daniel W. Fuller, and Simon J. Nicol (2025). *Reference Model of Skipjack Tuna in the Pacific Ocean Using SEAPODYM Integrating Catch, Length, Tagging, and Early Life History Data*. Information Paper WCPFC-SC21-2025/SA-IP-20. WCPFC.

Forestier, Romain, Lucas Bonnin, Inna Senina, Tiffany Vidal, Marc Ghergariu, and Simon Nicol (2026). "A comprehensive method to integrate unbiased fisheries data in spatially-explicit population dynamics models". In: *In prep.*

OFP-SPC (2026). *PROJECT 42: PACIFIC TUNA TAGGING PROJECT REPORT AND WORK-PLAN FOR 2026-2029 — WCPFC Meetings*. Research Paper. 22nd Regular Session of the Scientific Committee.

Senina, Inna, Lucas Bonnin, Romain Forestier, Matthieu Lengaigne, Karen Guihou, Julien Temple-Bouyer, and Simon Nicol (2026a). *SEAPODYM Applications to Pacific Tuna Species*. WCPFC Scientific Committee Information Paper WCPFC-SC22-2026/EB-IP-03. Presented at the 22nd Regular Session of the Scientific Committee of the Western and Central Pacific Fisheries Commission, 11–19 August 2026. Apia, Samoa: Western and Central Pacific Fisheries Commission (WCPFC).

Senina, Inna, Lucas Bonnin, Forestier Romain, and Simon J. Nicol (2026b). *Advancing the SEAPODYM modeling framework: methodology, validation, and analyses*. Working Paper WCPFC-SC22-2026/EB-WP-01. WCPFC.

7 Appendix

7.1 Tables

Table 2: Definitions and notations of model parameters.

Parameter	Description
	Recruitment
r	Reproduction rate in Beverton–Holt function, in mo^{-1}
b	Slope parameter in Beverton–Holt function, in $\mathrm{Nb/km}^2$
	Natural mortality
$\bar{m}_p$	Predation mortality rate at age 0, in mo^{-1}
β_p	Slope coefficient in predation mortality
$\bar{m}_s$	Senescence mortality rate at age 0, in $\mathrm{mo}^{-1-\beta_s}$
β_s	Slope coefficient in senescence mortality
ϵ_a	Variability of mortality rate with habitat index from M in the best habitat to $M(1+\epsilon)$ in the worst habitat
ϵ_0	Variability of larvae mortality rate with habitat index from M in the best habitat to $M(1+\epsilon)$ in the worst habitat
	Spawning habitat H_s
σ_1	Slope of increased temperature suitability in double logistic threshold larvae thermal suitability
σ_2	Slope of decreased temperature suitability in double logistic threshold larvae thermal suitability
$T_1^\star$	Minimal temperature threshold in double logistic threshold larvae thermal suitability
$T_2^\star$	Maximal temperature threshold in double logistic threshold larvae thermal suitability
α_P	Prey encounter rate in Holling type III function, in day^{-1}
α_F	Log-normal mean parameter in predator-dependent function, in $\mathrm{g\,m}^{-2}$
β_F	Log-normal shape parameter in predator-dependent function
	Adult feeding habitat H_a
σ_0	Standard deviation in temperature Gaussian function for age 0
σ_m	Standard deviation in temperature Gaussian function at age A+, in °C
T_0	Preferred temperature for age 0
T_m	Preferred temperature for the oldest adult class A+, in °C
b_T	Allometric power coefficient for thermal preferences at age
γ	Slope in the oxygen accessibility function
$\hat{O}$	Minimal threshold oxygen value required by the predator to access feeding habitat, in $\mathrm{ml\,L}^{-1}$
E_{11}	Contribution of epipelagic forage to the feeding habitat index
E_{22}	Contribution of mesopelagic forage to the feeding habitat index
E_{21}	Contribution of migrant mesopelagic forage to the feeding habitat index
E_{33}	Contribution of lower mesopelagic forage to the feeding habitat index
E_{32}	Contribution of migrant lower mesopelagic forage to the feeding habitat index
E_{31}	Contribution of highly migrant lower mesopelagic forage to the feeding habitat index
	Movement
A	Slope coefficient in allometric function for tuna velocity
V_m	Maximum sustainable swimming speed (taxis), $\mathrm{BL\,s}^{-1}$
σ	Diffusion-rate multiplier
c	Diffusion–habitat coefficient
	Fisheries
q_{t0}^f	Constant catchability coefficient for fishery f
b^f	Slope of catchability linear trend with time for fishery f
ς_f	Slope coefficient in sigmoid-shape selectivity (type II selectivity)
$\tilde{l}_f$	Threshold length in sigmoid-shape selectivity (type II selectivity); mean length in type III selectivity
σ_f	Standard deviation in type III selectivity
μ_f	Asymptotic value of selectivity in the type III function

Table 3: Best solution model parameters. Asterisks indicate when the parameter was estimated close to its minimum (*) or maximum (**) bound. A short description of parameters is provided by refer to Table 2 for more details.

Par.	Description	Min	Max	Value
r	reproduction rate in Bev.-Holt function	0.05	0.95	0.065*
b	slope parameter in Bev.-Holt function	0.01	20	10.1
$\bar{m}_p$	predation mortality rate, mo^{-1}	0	0.15	0.13
β_p	predation mortality slope, mo^{-1}	0.01	0.5	0.382
$\bar{m}_s$	senescence mortality rate, mo^{-1}	0	0.006	0.0000458*
β_s	senescence mortality slope, mo^{-1}	0.5	1.7	1.42
ϵ_a	habitat-dependent mortality amplitude	0.05	5	4.97**
ϵ_0	larval habitat-dependent mortality amplitude	0	30	4.74
q_{larvae}	larvae catchability	0	100	0.0796*
σ_{larvae}	first slope in thermal suitability, °C	0.01	0.6	0.6**
T_{larvae}	first SST threshold in thermal suitability, °C	15	27.5	19.3
$\sigma_{2larvae}$	second slope in thermal suitability, °C	0.01	0.6	0.0102*
$T_{2larvae}$	second SST threshold in thermal suitability, °C	28	32	32**
α_P	prey (NPP) function shape (Holling III)	0	5	0.0454*
α_F	predation function amplitude	0	5	4.74
β_F	predation function shape	0	5	3.28
σ_0	SST-Gaussian std. dev., age 0, °C	0.01	2.5	0.0312*
σ_m	SST-Gaussian std. dev., oldest cohort, °C	0.1	15	4.48
T_0	optimal SST, age 0, °C	26	38	29.2
T_m	optimal SST, oldest cohort, °C	10	36	26.6
b_T	thermal-preference age slope	1	3	3**
γ	oxygen response slope	0.0001	0.125	0.0001*
$\hat{O}$	oxygen threshold, $ml.L^{-1}$	0	4	1.8
$E_{1,1}$	epi. forage contrib.	0.05	10	1.72
$E_{2,2}$	upper meso. forage contrib.	0.05	10	10**
$E_{2,1}$	migrant up. meso. forage contrib.	0.05	10	0.0869*
$E_{3,3}$	lower meso. forage contrib.	0	20	0*
$E_{3,2}$	mig. l. meso. forage contrib.	0	20	0.000000168*
$E_{3,1}$	hmig. l. meso. forage contrib.	0.05	1	0.87
ϱ_s	start of spawning season	0.95	1.4	1.4**
$\hat{t}$	peak spawning date	0	365	128
A	maximum sustainable speed (taxis), $BL.s^{-1}$	0.85	1.1	0.85*
V_m	maximum advection velocity	0.1	2	0.211
σ	diffusion-rate multiplier	0	2	0.5
c	diffusion-habitat coefficient	0	1	0.000000000185*
q_{t0}^{P14}	Catch. for P14	0	0.5	0.0554
b^{P14}	Catch. slope for P14	-0.0001	0.001	0.001**
q_{t0}^{L16}	Catch. for L16	0	0.1	0.00246*
b^{L16}	Catch. slope for L16	-0.0001	0.001	0.000000523
q_{t0}^{L17}	Catch. for L17	0	0.1	0.000774*

b^{L17}	Catch. slope for L17	-0.0001	0.001	-0.000000392
q_{t0}^{L18}	Catch. for L18	0	0.1	0.00131*
b^{L18}	Catch. slope for L18	-0.0001	0.001	-0.000000924
q_{t0}^{L19}	Catch. for L19	0	0.1	0.00388*
b^{L19}	Catch. slope for L19	-0.0001	0.001	-0.00000238
q_{t0}^{L20}	Catch. for L20	0	0.1	0.00135*
b^{L20}	Catch. slope for L20	-0.0001	0.001	-0.00000289
q_{t0}^{L21}	Catch. for L21	0	0.1	0.00146*
b^{L21}	Catch. slope for L21	-0.0001	0.001	-0.00000169
q_{t0}^{P110}	Catch. for P110	0	0.5	0.203
b^{P110}	Catch. slope for P110	-0.0001	0.001	-0.0001*
q_{t0}^{P111}	Catch. for P111	0	0.5	0.128
b^{P111}	Catch. slope for P111	-0.0001	0.001	-0.0000929*
q_{t0}^{S1}	Catch. for S1	0	0.1	0.0393
q_{t0}^{S2}	Catch. for S2	0	0.1	0.0847
q_{t0}^{S3}	Catch. for S3	0	0.1	0.00049*
q_{t0}^{S4}	Catch. for S4	0	0.1	0.0104
q_{t0}^{S5}	Catch. for S5	0	0.1	0.0485
q_{t0}^{S6}	Catch. for S6	0	0.1	0.00416*
q_{t0}^{S7}	Catch. for S7	0	0.1	0.0426
q_{t0}^{S8}	Catch. for S8	0	0.1	0.0626
q_{t0}^{P9}	Catch. for P9	0	0.1	0.0832
b^{P9}	Catch. slope for P9	-0.0001	0.001	0
q_{t0}^{P10}	Catch. for P10	0	0.1	0.0598
b^{P10}	Catch. slope for P10	-0.0001	0.001	0
q_{t0}^{P12}	Catch. for P12	0	0.1	0.0000245*
b^{P12}	Catch. slope for P12	-0.0001	0.001	-0.0001*
q_{t0}^{P13}	Catch. for P13	0	0.1	0.1**
b^{P13}	Catch. slope for P13	-0.0001	0.001	0.001**
q_{t0}^{O15}	Catch. for O15	0	0.1	0.0515
ς_{S1}	Std. dev. for S1 sel.	0.05	15	3.34
ς_{S2}	Std. dev. for S2 sel.	0.05	15	5.09
ς_{S3}	Std. dev. for S3 sel.	0.05	15	10.1
ς_{S4}	Std. dev. for S4 sel.	0.05	15	8.86
ς_{S5}	Std. dev. for S5 sel.	0.05	15	11.3
ς_{S6}	Std. dev. for S6 sel.	0.05	15	19.5**
ς_{S7}	Std. dev. for S7 sel.	0.05	15	3.61
ς_{S8}	Std. dev. for S8 sel.	0.05	15	9.55
ς_{P9}	Std. dev. for P9 sel.	0.05	15	0.997
ς_{P10}	Std. dev. for P10 sel.	0.05	15	0.997
ς_{P12}	Std. dev. for P12 sel.	0.05	15	0.997
ς_{P13}	Std. dev. for P13 sel.	0.05	15	0.997
ς_{P14}	Std. dev. for P14 sel.	0.05	15	11.2
ς_{O15}	Std. dev. for O15 sel.	0.05	1	0.128

ς_{L16}	Std. dev. for L16 sel.	0.05	1	0.15
ς_{L17}	Std. dev. for L17 sel.	0.05	1	0.121
ς_{L18}	Std. dev. for L18 sel.	0.05	1	0.361
ς_{L19}	Std. dev. for L19 sel.	0.05	1	0.124
ς_{L20}	Std. dev. for L20 sel.	0.05	1	0.118
ς_{L21}	Std. dev. for L21 sel.	0.05	1	0.104
ς_{P110}	Std. dev. for P110 sel.	0.05	15	0.24*
ς_{P111}	Std. dev. for P111 sel.	0.05	15	15**
$\hat{l}_{S1}$	Threshold (II) or mean length (III) S1 sel.	22.5	152	48
μ_{S1}	Asympt. val. for S1 sel.	0	1	1**
$\hat{l}_{S2}$	Threshold (II) or mean length (III) S2 sel.	22.5	152	48
μ_{S2}	Asympt. val. for S2 sel.	0	1	1**
$\hat{l}_{S3}$	Threshold (II) or mean length (III) S3 sel.	22.5	152	50
μ_{S3}	Asympt. val. for S3 sel.	0	1	0.466
$\hat{l}_{S4}$	Threshold (II) or mean length (III) S4 sel.	22.5	152	48
μ_{S4}	Asympt. val. for S4 sel.	0	1	1**
$\hat{l}_{S5}$	Threshold (II) or mean length (III) S5 sel.	22.5	152	58
μ_{S5}	Asympt. val. for S5 sel.	0	1	1**
$\hat{l}_{S6}$	Threshold (II) or mean length (III) S6 sel.	22.5	152	48
μ_{S6}	Asympt. val. for S6 sel.	0	1	1**
$\hat{l}_{S7}$	Threshold (II) or mean length (III) S7 sel.	22.5	152	48
μ_{S7}	Asympt. val. for S7 sel.	0	1	1**
$\hat{l}_{S8}$	Threshold (II) or mean length (III) S8 sel.	22.5	152	58
μ_{S8}	Asympt. val. for S8 sel.	0	1	0.927
$\hat{l}_{P9}$	Threshold (II) or mean length (III) P9 sel.	22.5	152	49.1
μ_{P9}	Asympt. val. for P9 sel.	0	1	0.5
$\hat{l}_{P10}$	Threshold (II) or mean length (III) P10 sel.	22.5	152	49.1
μ_{P10}	Asympt. val. for P10 sel.	0	1	0.5
$\hat{l}_{P12}$	Threshold (II) or mean length (III) P12 sel.	22.5	152	49.1
μ_{P12}	Asympt. val. for P12 sel.	0	1	1**
$\hat{l}_{P13}$	Threshold (II) or mean length (III) P13 sel.	22.5	152	49.1
μ_{P13}	Asympt. val. for P13 sel.	0	1	1**
$\hat{l}_{P14}$	Threshold (II) or mean length (III) P14 sel.	22.5	152	46
μ_{P14}	Asympt. val. for P14 sel.	0	1	1**
$\hat{l}_{O15}$	Threshold (II) or mean length (III) O15 sel.	22.5	152	27.8*
$\hat{l}_{L16}$	Threshold (II) or mean length (III) L16 sel.	22.5	152	92.2
$\hat{l}_{L17}$	Threshold (II) or mean length (III) L17 sel.	22.5	152	101
$\hat{l}_{L18}$	Threshold (II) or mean length (III) L18 sel.	22.5	152	89.8
$\hat{l}_{L19}$	Threshold (II) or mean length (III) L19 sel.	22.5	152	98.9
$\hat{l}_{L20}$	Threshold (II) or mean length (III) L20 sel.	22.5	152	104
$\hat{l}_{L21}$	Threshold (II) or mean length (III) L21 sel.	22.5	152	89.4
$\hat{l}_{P110}$	Threshold (II) or mean length (III) P110 sel.	22.5	152	28.7*
μ_{P110}	Asympt. val. for P110 sel.	0	1	0.174
$\hat{l}_{P111}$	Threshold (II) or mean length (III) P111 sel.	22.5	152	104

μ_{P111}	Asympt. val. for P111 sel.	0	1	0.174

Table 4: Description of the 22 fisheries and associated catch data. Resolution of catch data, and methods used for catch prediction for individual fisheries are indicated.

Fishery	**Gear type**	**Definition**	**Pred. method**	**Res.**
S1	Purse-seine	Subtropics North West	Catch-Removal	1°
S2	Purse-seine	West tropics, free schools	Catch-Removal	1°
S3	Purse-seine	West tropics, floating objects	Catch-Removal	1°
S4	Purse-seine	EPO, floating objects	Catch-Removal	1°
S5	Purse-seine	Dolphin-associated	Catch-Removal	1°
S6	Purse-seine	Unreliable/Uncategorised	Catch-Removal	1°
S7	Purse-seine	EPO, free schools	Catch-Removal	1°
S8	Purse-seine	Whale shark associated	Catch-Removal	1°
P9	Pole-and-line	Japanese $\leq$ 1981	Gordon-Schaefer	1°
P10	Pole-and-line	Japanese 1982–1989	Gordon-Schaefer	1°
P110	Pole-and-line	Japanese 1990–2003	Gordon-Schaefer	1°
P111	Pole-and-line	Japanese 2006	Gordon-Schaefer	1°
P12	Pole-and-line	Southern Ocean (<25°S)	Gordon-Schaefer	1°
P13	Pole-and-line	Northern EPO	Gordon-Schaefer	1°
P14	Pole-and-line	All other pole-and-line	Gordon-Schaefer	1°
O15	Other	All other gears	Catch-Removal	5°
L16	Longline	Cluster 1 from detailed data (YFT-target)	Gordon-Schaefer	1°
L17	Longline	Cluster 2 from detailed data (BET-target)	Gordon-Schaefer	1°
L18	Longline	Cluster 3 from detailed data (ALB-target)	Gordon-Schaefer	1°
L19	Longline	Cluster 1 from raised data (YFT-target)	Gordon-Schaefer	5°
L20	Longline	Cluster 2 from raised data (BET-target)	Gordon-Schaefer	5°
L21	Longline	Cluster 3 from raised data (ALB-target)	Gordon-Schaefer	5°

7.2 Figures

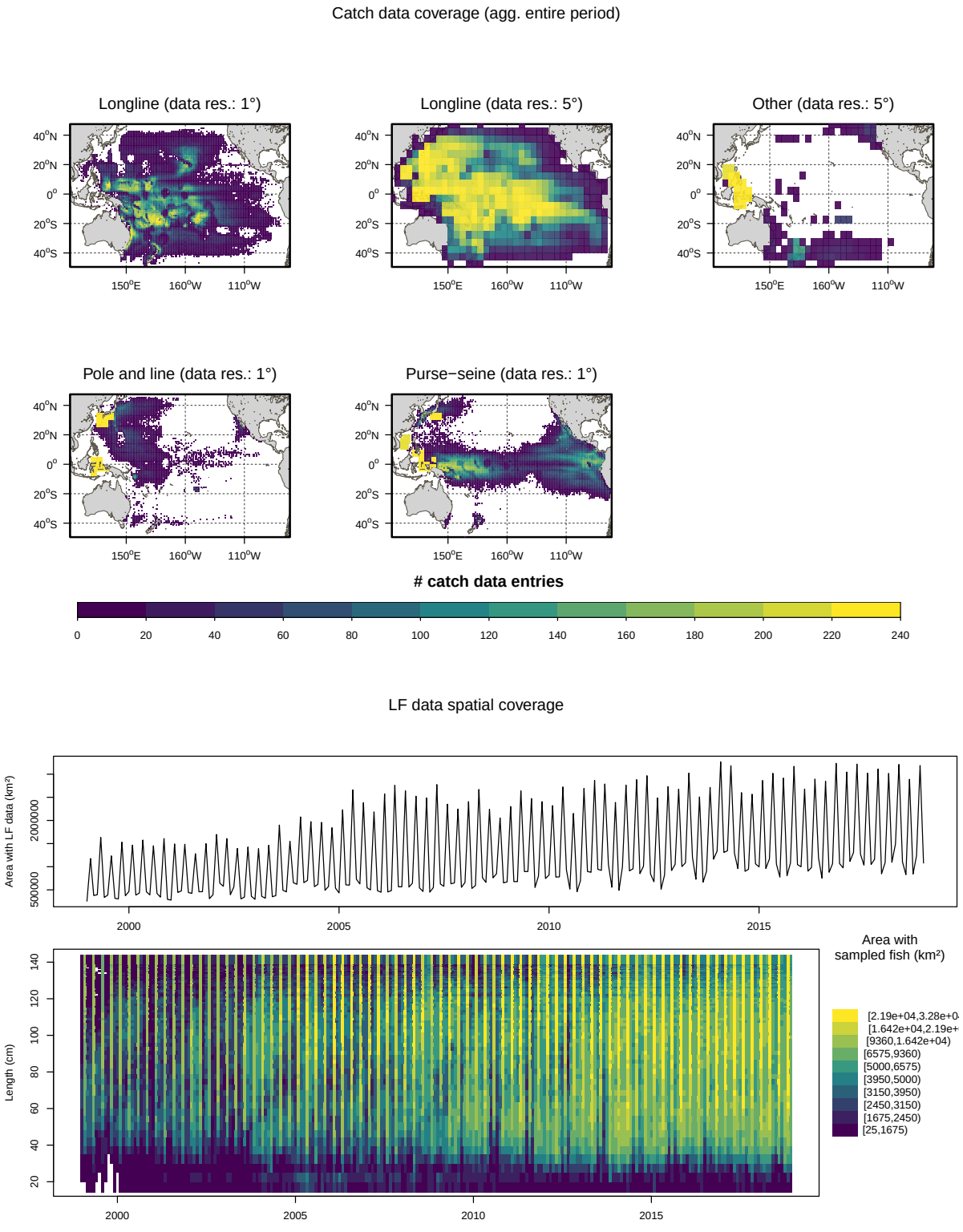

Figure 20: Fisheries data coverage over the period used for MLE (1998-2018)

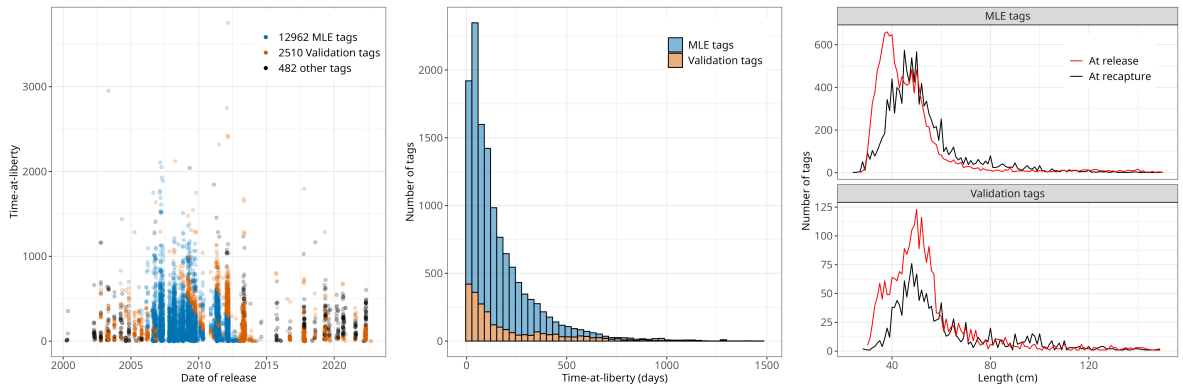

Figure 21: Conventional tagging data. The history of tag releases and time-at-liberty for the MLE dataset and the validation dataset is displayed on the left panel. The center panel shows the dsitribution of time-at-liberty. The right panel shows the distribution of length at release and recapture, for the MLE and the validation dataset.

(a) Adult distribution: INTERIM reference model vs interm. CL MLE

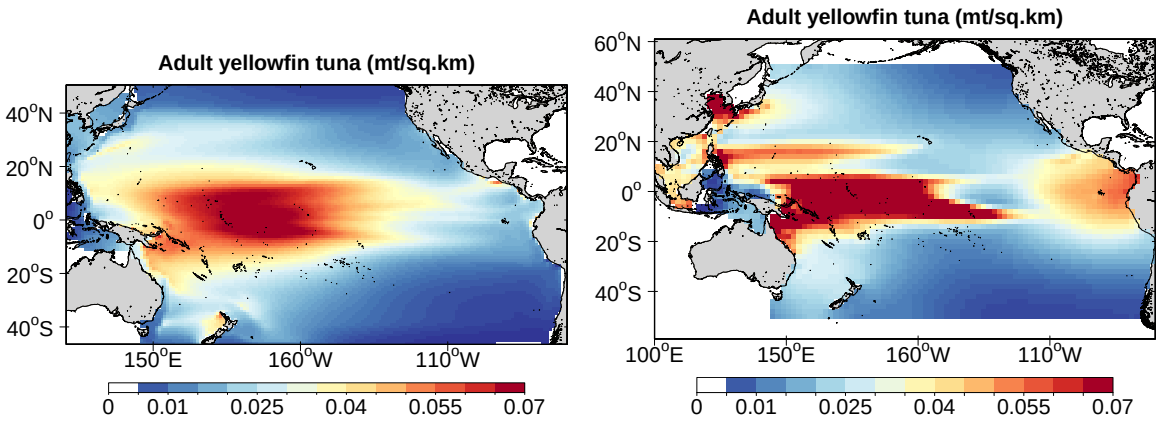

(b) First Intermediate CLT MLE: Unrealistic thermal suitability and lack of EPO adult biomass

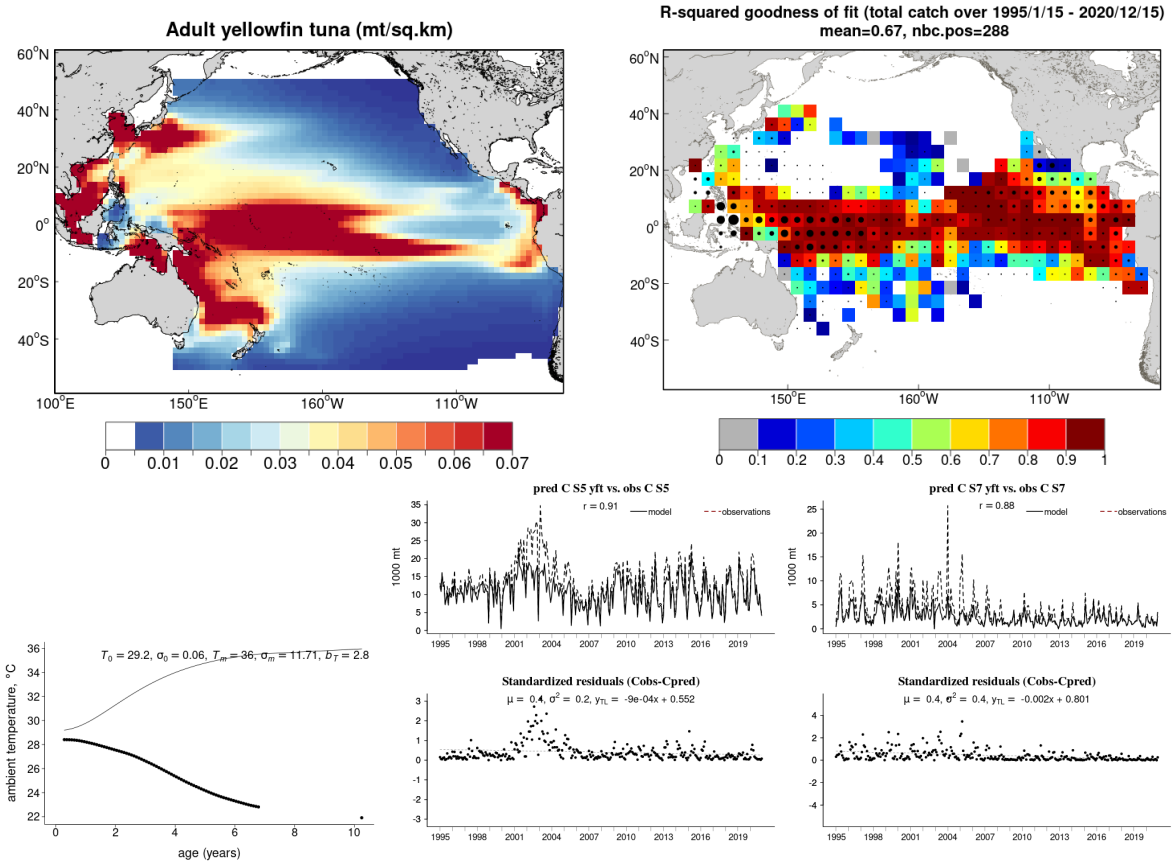

Figure 22
continued. . .

Figure 22 continued

(c) Second Intermediate CLT MLE: Improvement of thermal suitability and EPO biomass

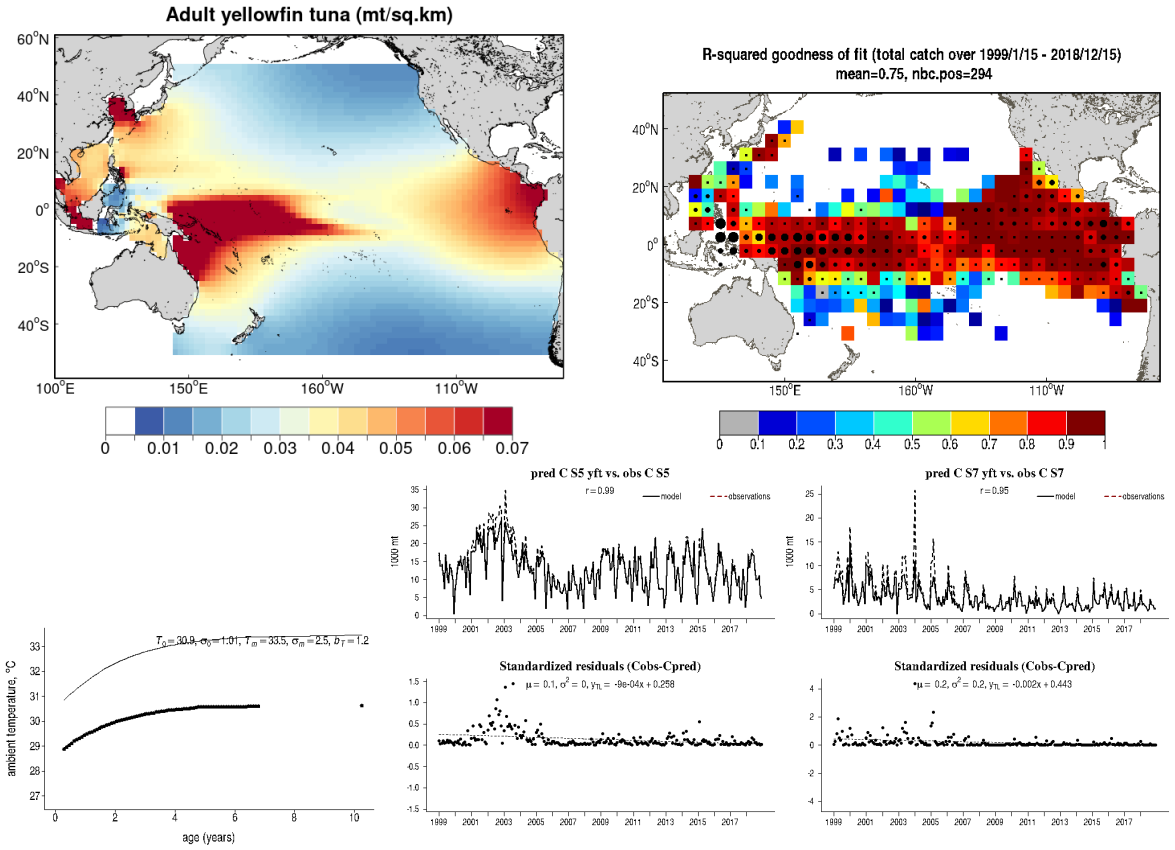

(d) Effect of less restrictive bounding of mortality parameters on MLE

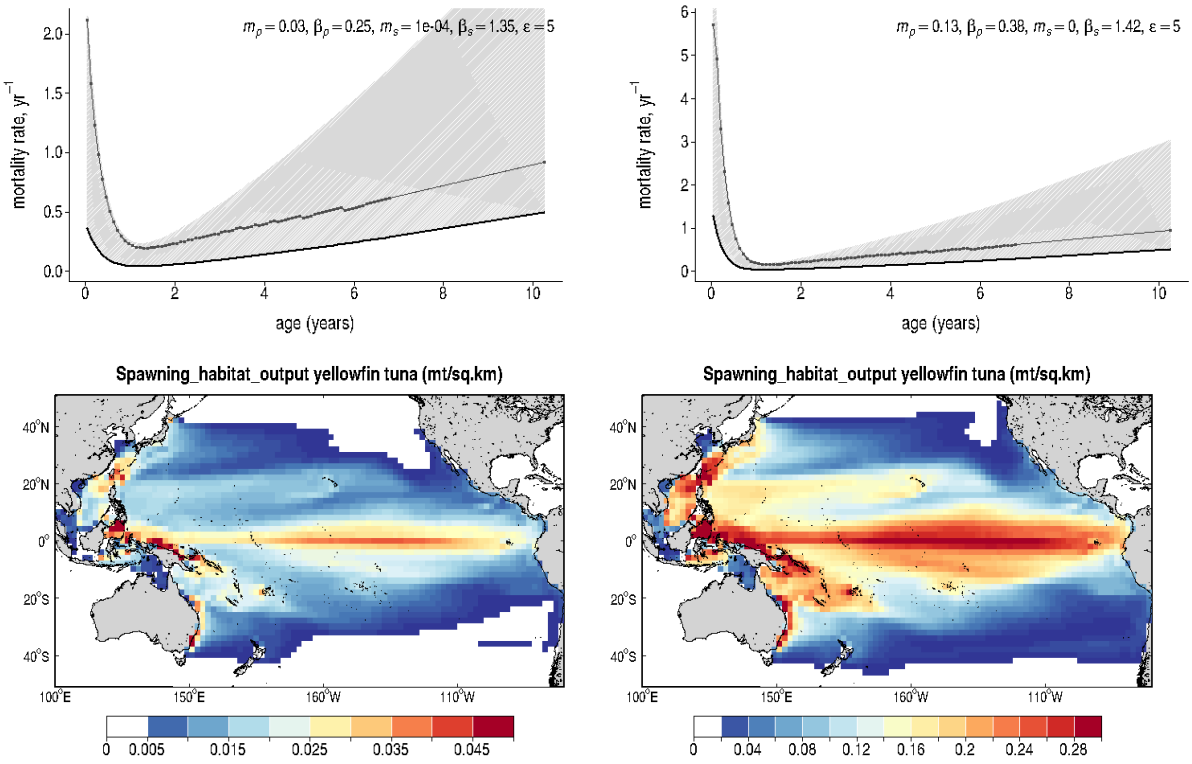

Figure 22: Various examples of improvements along model development

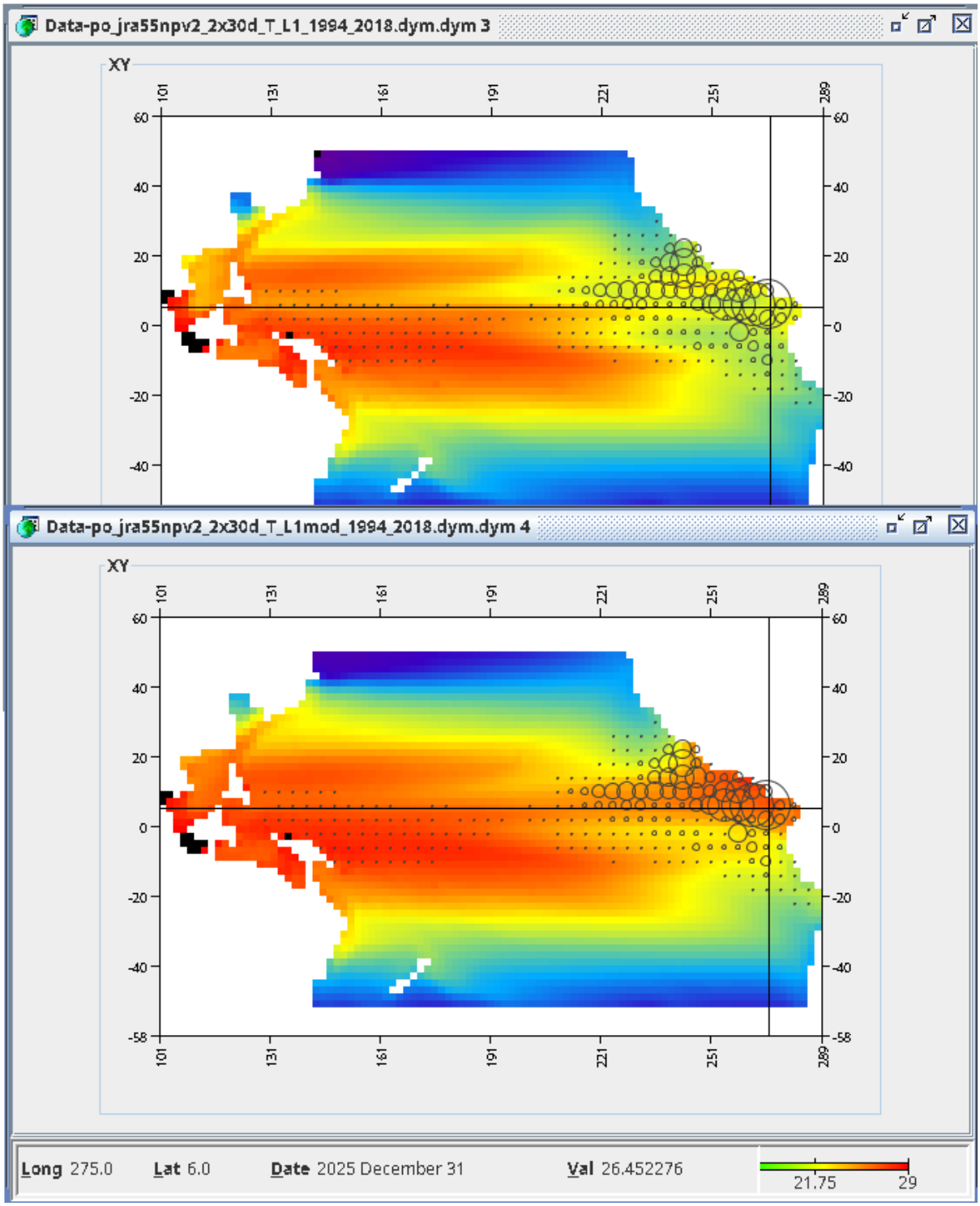

Figure 23: Correction of epipelagic temperature field. Black circles represent observed catch in the unassociated purse-seine fishery (S5)

(a) Length frequencies

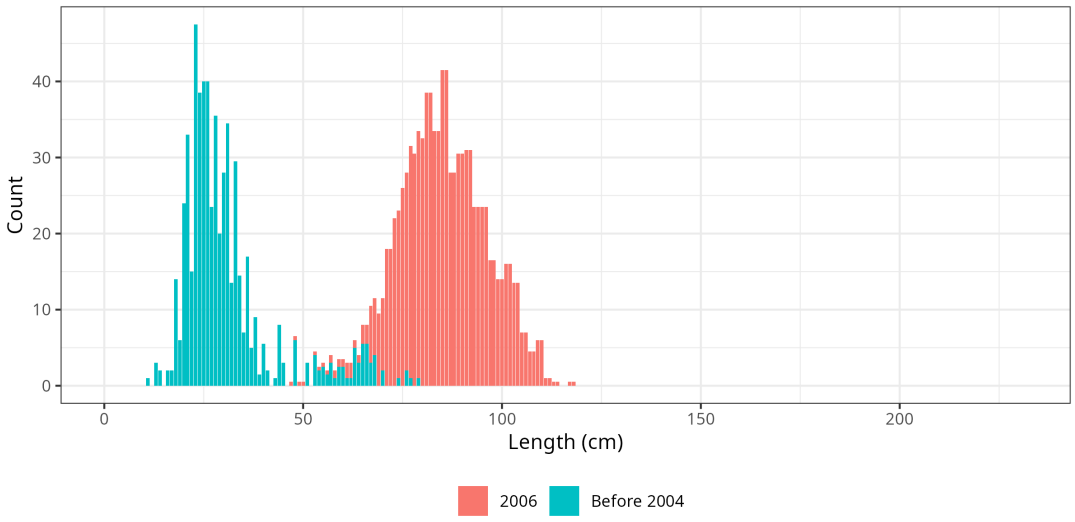

(b) Mean length

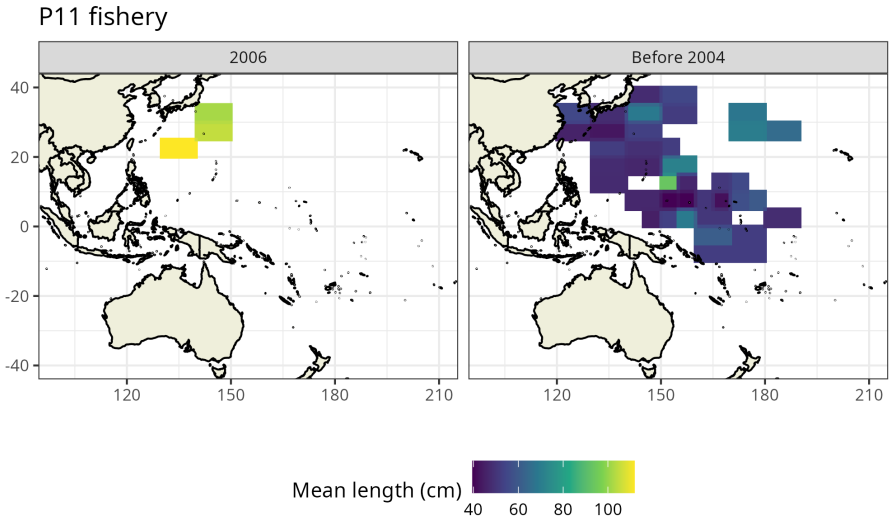

Figure 24: Discrepancies in the P11 fishery leading to a split into P110 and P111.

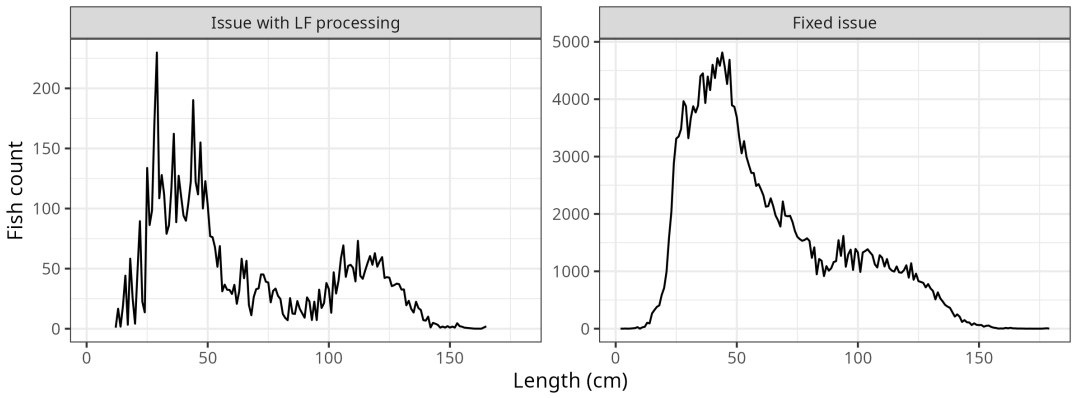

Figure 25: Issue with the processing of length-frequencies and its impact on S7 fisheries data.

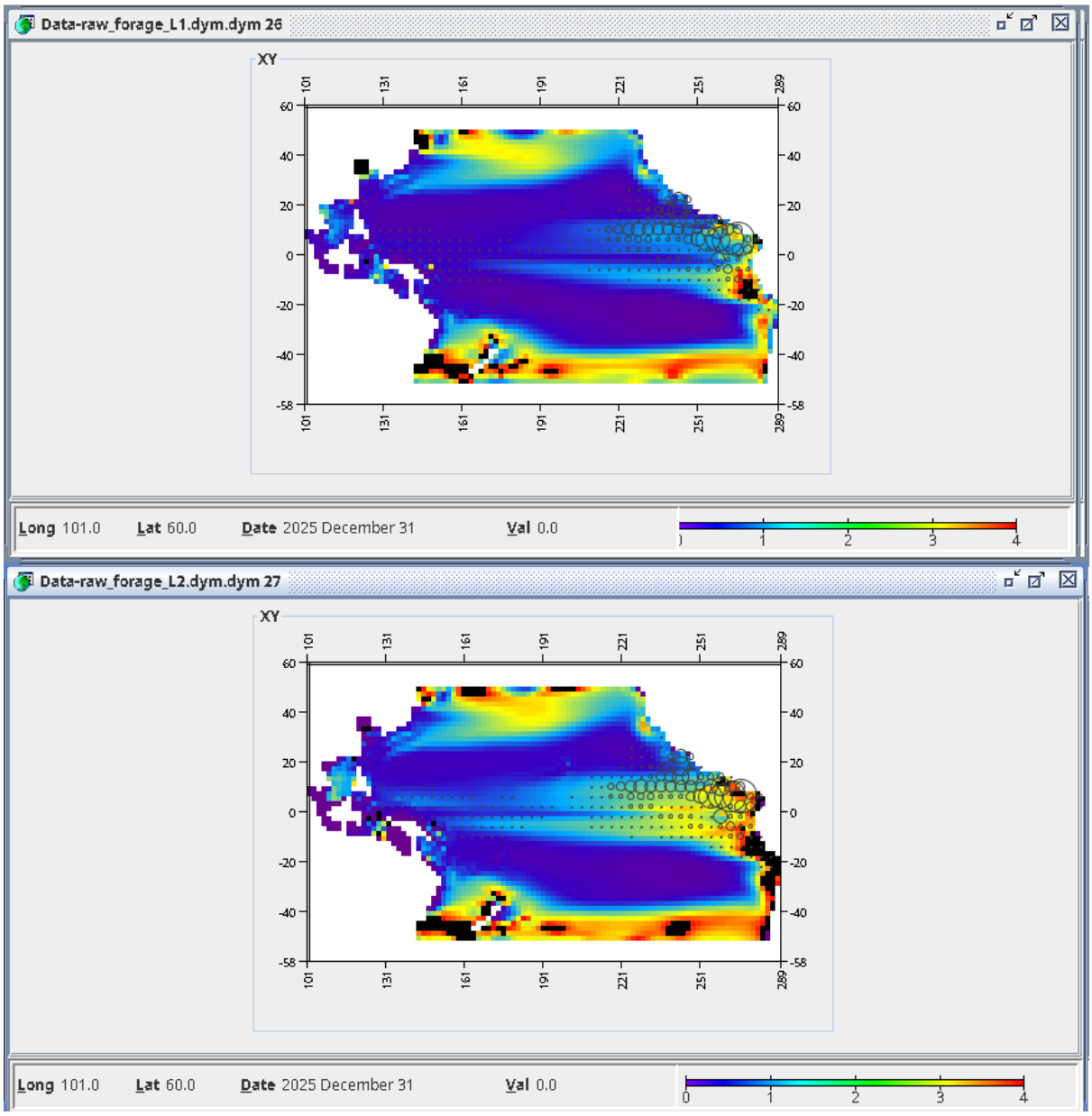

Figure 26: Raw forage in epipelagic and upper-mesopelagic layers. Black circles represent observed catch in the unassociated purse-seine fishery (S5)

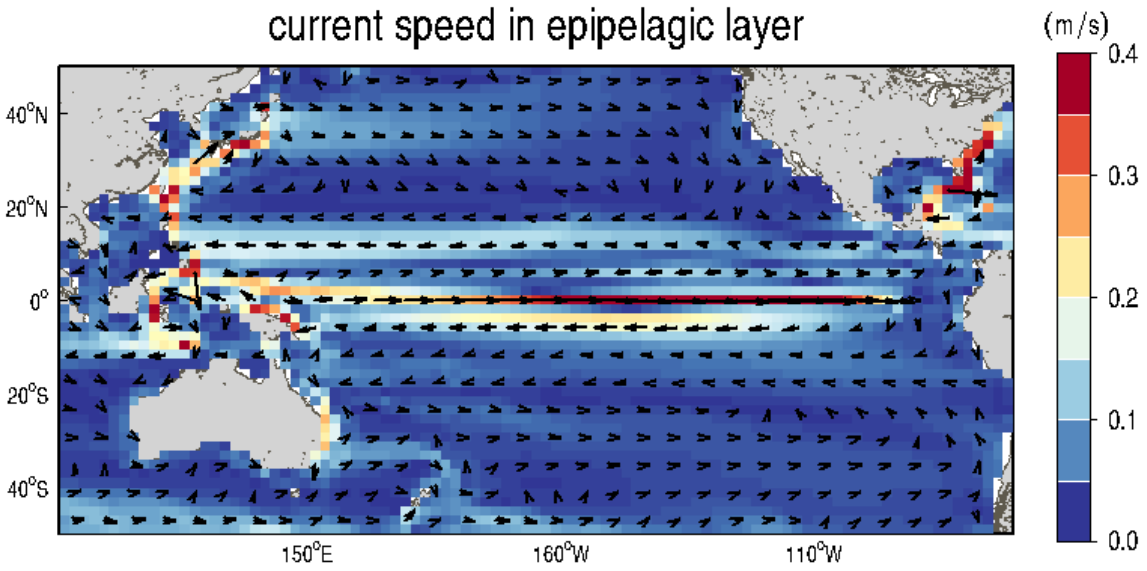

Figure 27: Horizontal currents in the epipelagic layer.

(a) Feeding habitat index

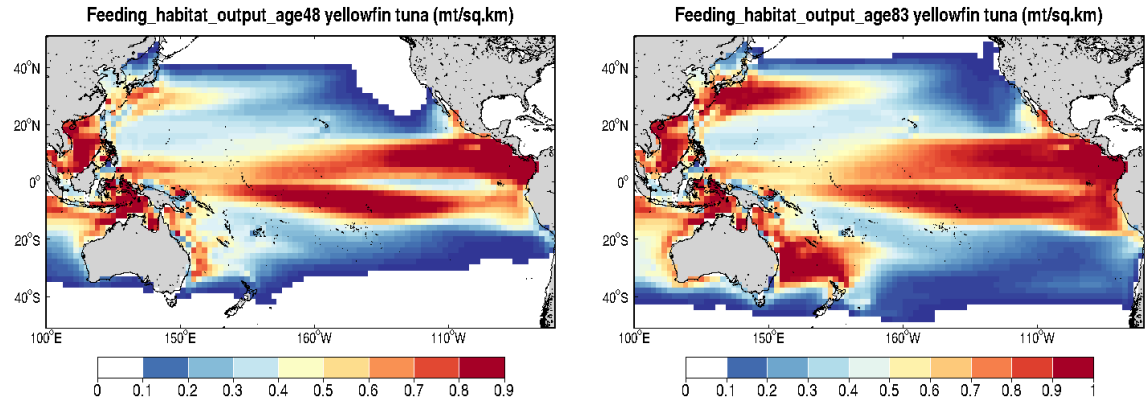

(b) Layer contribution to feeding habitat index

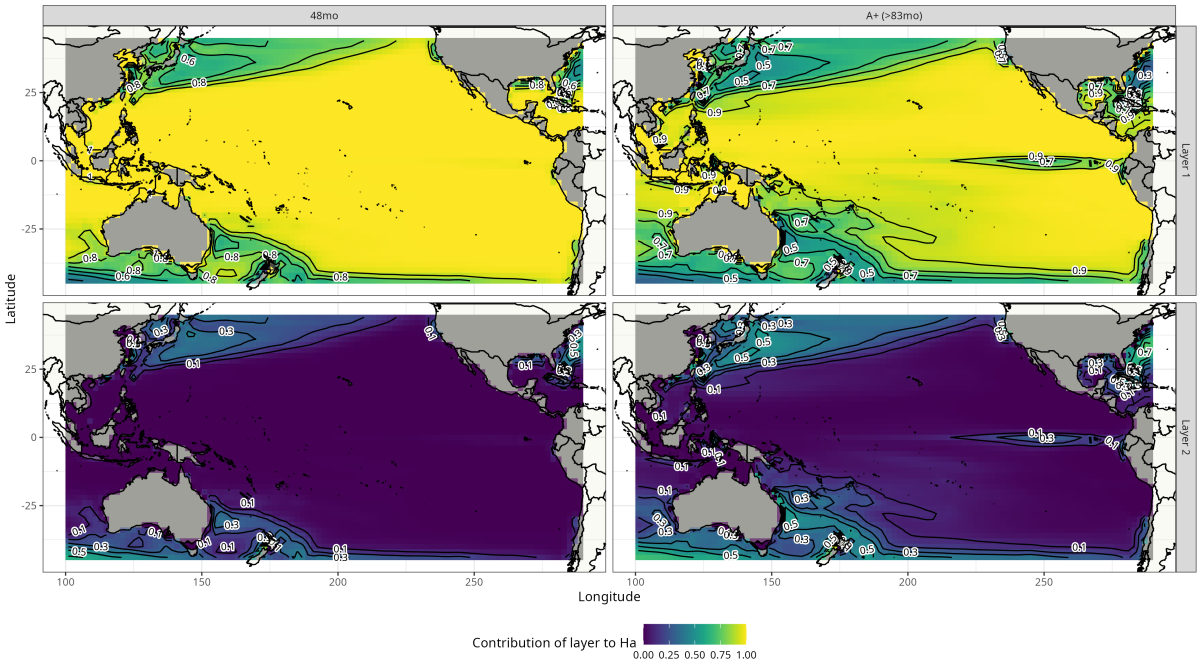

Figure 28: Contribution of vertical layers to feeding habitat. For each age class, the contribution of each of the three vertical layers to the feeding habitat index can be computed as the proportion of accessible forage in the layer. Here, only layer 1 (epipelagic layer) and 2 (upper mesopelagic) are displayed, as the lower mesopelagic layer does not contribute to feeding habitat.

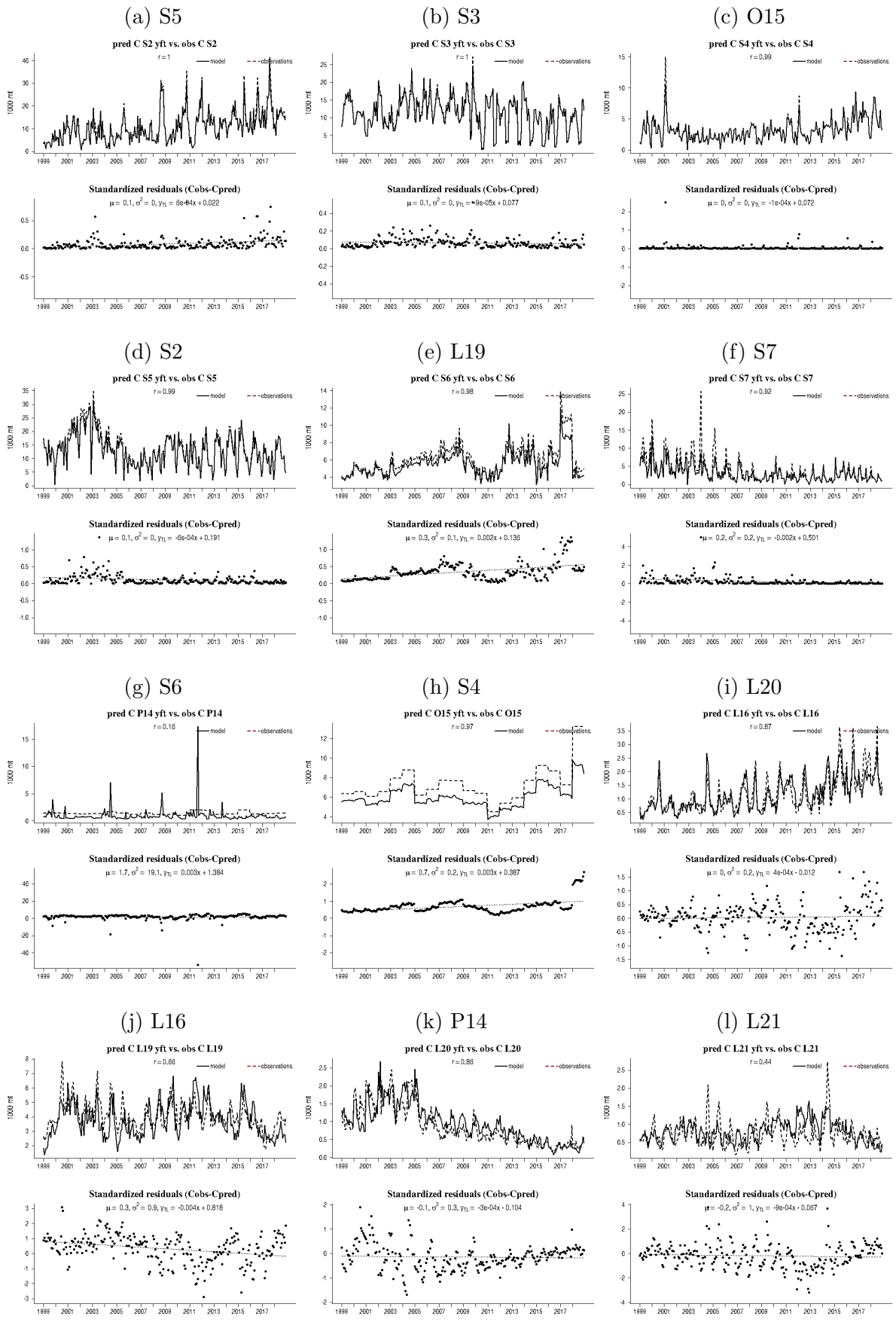

Figure 29: Fisheries-specific observed versus predicted catch, aggregated over the full spatial scale. Only fisheries that represent more than 1% of total catch are displayed here

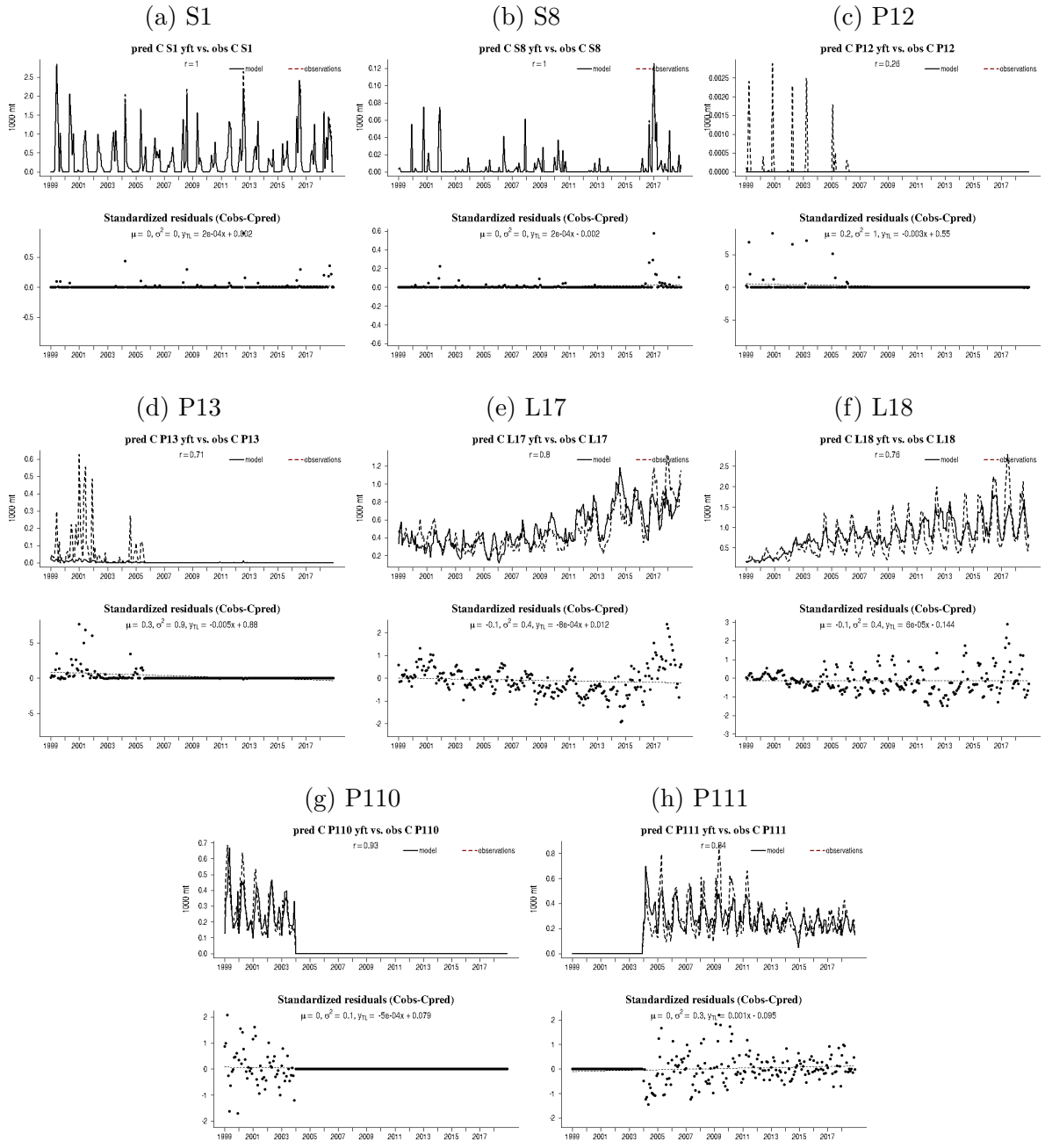

Figure 30: Fisheries-specific observed versus predicted catch, aggregated over the full spatial scale. Only fisheries that represent less than 1% of total catch are displayed here

(a) MLE dataset - 1999-2018

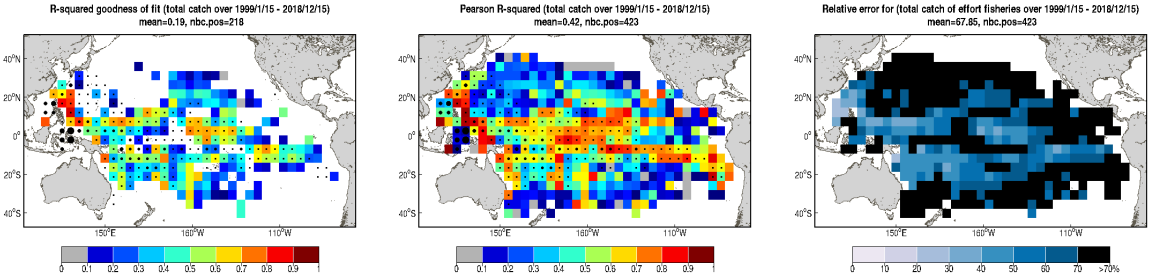

(b) Validation dataset - 1983-1998

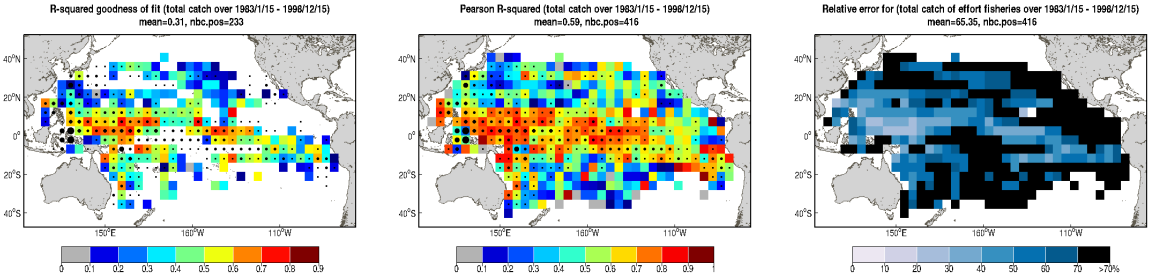

(c) Validation dataset - 2019-2022

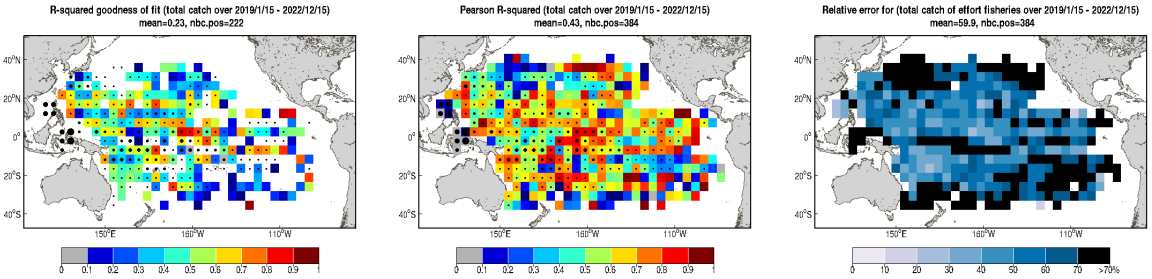

Figure 31: Maps of fit metrics - effort-based fisheries only.

(a) 1970-1979

(b) 2010-2019

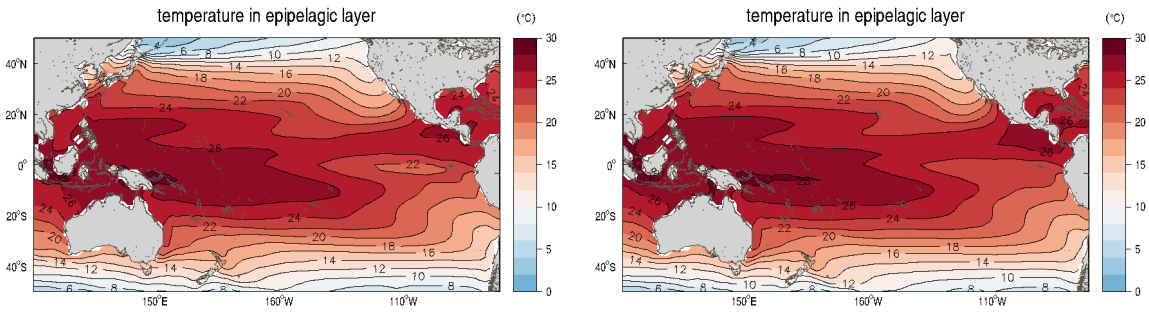

Figure 32: Evolution of epipelagic temperature between the 1970's and the 2010's.

7.3 Correction of the epipelagic temperature

The corrected epipelagic layer temperature T_{L1}^{cor} is defined as:

$$T_{L1}^{cor} = T_{L1} + 4\, dT_z\, (\mathrm{SST} - T_{L1}) \tag{5}$$

with dT_z a proxy for vertical thermal gradient, defined as:

$$dT_z = \min\left(0.2, \max\left(0, \frac{2(\mathrm{SST} - T_{L1})}{Z_{eu}}\right)\right) \tag{6}$$